1 **Characterization of smoke/dust episode over West Africa: comparison of MERRA-2**

2 **modeling with multiwavelength Mie-Raman lidar observations**

3 Igor Veselovskii[1,2,3], Philippe Goloub[4], Thierry Podvin[4], Didier Tanre[4], Arlindo da Silva[3], Peter

4 Colarco[3], Patricia Castellanos[3,5], Mikhail Korenskiy[1], Qiaoyun Hu[3], David N. Whiteman[4], Daniel

5 Pérez-Ramírez[6], Patrick Augustin[7], Marc Fourmentin[7], Alexei Kolgotin[1]

6 [1]*Physics Instrumentation Center of GPI, Troitsk, Moscow, Russia.*

7 [2]*Joint Center for Earth Systems Technology, UMBC, Baltimore, USA*

8 [3]*NASA Goddard Space Flight Center, Greenbelt, USA*

9 [4]*Laboratoire d'Optique Atmosphérie, Université de Lille-CNRS, Villeneuve d'Ascq, France*

10 [5]*Universities Space Research Association, Columbia, Maryland, USA*

11 [6]*Applied Physics Department, University of Granada, Spain*

12 [7]*Laboratoire de Physico-chimie de l'atmosphère, Université du littoral côte d'Opale, France*

14 **Abstract**

15 Observations of multiwavelength Mie-Raman lidar taken during the SHADOW field

16 campaign are used to analyze a smoke/dust episode over West Africa on 24-27 December 2015.

17 For the case considered, the dust layer extended from the ground up to approximately 2000 m

18 while the elevated smoke layer occurred in the 2500 m – 4000 m range. The profiles of lidar

19 measured backscattering, extinction coefficients and depolarization ratios are compared with the

20 vertical distribution of aerosol parameters provided by the Modern-Era Retrospective analysis

21 for Research and Applications, Version 2 (MERRA-2). The MERRA-2 model simulated the

22 correct location of the near–surface dust and elevated smoke layers. The values of modeled and

23 observed extinctions at both 355 nm and 532 nm are also rather close. Good coherence between

24 measured and modeled extinction profiles provides an opportunity to test how well the model

25 reproduces backscattering of dust particles at different wavelengths. The comparison shows good

26 agreement of modeled and measured backscattering coefficients at 355 nm, meaning that the

27 modeled dust lidar ratio of 65 sr in the near-surface layer is close to the observed value. At 532

28 nm however, the simulated lidar ratio is lower than measurements (about 40 sr and 50 sr

29 respectively). The reason for this disagreement could be that the assumed imaginary part of the

30 refractive index for dust (0.0025 at 532 nm) is too low, or that the particle size distribution in the

31 model is too much weighted toward fine mode dust. The model predicts significant concentration

of dust particles inside the smoke layer. This is supported by a high depolarization ratio of 15%
observed in the center of this layer. The backscattering Ångström exponent at 355/532 nm as
well as both lidar ratios have a minimum in the center of the elevated layer, which can also be
explained by the presence of dust.

1. Introduction

Atmospheric aerosols are an important factor influencing the Earth's radiative budget,
though its impact is still highly uncertain due largely to the complicated mechanisms of aerosol –
cloud interaction. In particular, the processes in the aerosol – cloud ecosystem are strongly
influenced by the height distribution of different aerosol components, thus the knowledge of
these height distributions is essential to decrease the uncertainty of aerosol radiative forcing
estimates. Lidar is a recognized instrument for vertical profiling of aerosol properties, and the
possibility to invert lidar observations at several wavelengths to aerosol microphysical properties
has been extensively studied both theoretically and experimentally over the two past decades
(e.g. Müller et al., 1999; 2016; Veselovskii et al., 2002; Böckman et al, 2005). These studies
revealed the importance of using Raman or HSRL (high spectral resolution lidar) systems, which
allow independent measurements of aerosol extinction and backscattering coefficients to be
made. At present, the most practical configuration of Raman (HSRL) lidar is based on a triple
Nd:YAG laser. Such a lidar provides the so called $3\beta+2\alpha$ set of observations, including three
backscattering (355 nm, 532 nm, 1064 nm) and two extinction (355 nm, 532 nm) coefficients.

However the problem of inversion of $3\beta+2\alpha$ observations is underdetermined. As a result,
instead of a unique solution, a family of solutions should be considered, leading to an increase in
retrieval uncertainties. Still the estimation of volume density (V) and effective radius (r_{eff}) with
uncertainty below 30% is possible, especially when the fine mode in the particle size distribution
(PSD) is predominant (e.g. Veselovskii et al., 2004; Müller et al., 2005; 2016; Pérez-Ramírez et
al., 2013,). The refractive index (RI) can be also estimated from the measurements, although the
uncertainty of such estimation is significant: for the real part (m_R) of RI the uncertainty is
normally about ±0.05 and for the imaginary part (m_I) it is about 50% when $m_I>0.01$.
(Veselovskii et al., 2004; Müller et al., 2016). Proposed improvements of inversion schemes
were considered in recent publications (Chemyakin et al., 2014; Kolgotin et al., 2016), still these

1   improvements don't resolve the fundamental issue: the information content of 3β+2α

2   observations is insufficient to support exact solution of the problem and additional information

3   should be used in retrievals to improve the accuracy of the retrieved products (Veselovskii et al.,

4   2005; Burton et al., 2016; Kahnert and Andersson, 2017; Alexandrov and Mishchenko, 7).

5   We should recall also that in the inversion schemes considered, the refractive index is

6   normally assumed to be spectrally and size independent, which is generally not the case in the

7   atmosphere. Moreover, the volume density and effective radius obtained from 3β+2α

8   observations are attributed to the whole size distribution, which is of limited practical use,

9   because of the importance of characterizing the particle properties separately for the fine and

10   coarse modes. Considering these issues makes the inverse problem even more underdetermined,

11   emphasizing the need for additional input information.

12   One opportunity to get this additional information is combining the lidar observations

13   with aerosol transport models (Kahnert and Andersson, 2017). Models provide the vertical

14   distribution of mass mixing ratios of chemical aerosol components, which can be used as "initial

15   guess" in the inversion scheme. MERRA-2 offers a unique opportunity to provide such an

16   "initial guesses" of the vertical structure of aerosol chemical composition. MERRA-2 is

17   produced with NASA's global Earth system model, GEOS-5 (Goddard Earth Observing System

18   version 5) (Gelaro et al 2017) and includes an online coupling with the Goddard Chemistry,

19   Aerosol, Radiation and Transport model (GOCART), which allows for assimilation of aerosol

20   optical depth (AOD) from space borne and surface instruments such as MODIS, AVHRR,

21   MISR, and AERONET (Randles et al. 2017). The fundamental data that MERRA-2 provides are

22   vertical profiles of the mass mixing ratios of five aerosol components: dust, sea salt, black and

23   organic carbon, and sulfate aerosols. The main optical parameters related to lidar measurements,

24   such as aerosol extinction and backscattering coefficients can be calculated basing on these data.

25   The principal question arising, however, is how well the reanalysis reproduces independent

26   observations, and thus can provide a realistic initial guess for a lidar inversion scheme. Buchard

27   et al. (2017) and Randles et al (2017) extensively validated MERRA-2 with independent surface

28   and aircraft observations of particulate matter (PM2.5) and AOD, as well as space-based

29   observations of absorption aerosol optical depth and aerosol index, finding generally good

30   agreement between the observations and MERRA-2.

1   For global validation of the aerosol vertical distribution, the modeled profiles of

2   attenuated backscatter were compared to spaceborne Cloud–Aerosol Lidar with Orthogonal

3   Polarization (CALIOP) observations (Winker et al., 2009), and a good consistency between

4   simulations and observations was reported (Nowottnick et al., 2015, Buchard et al., 2017).

5   However, the utility of CALIOP observations for accurate evaluation of aerosol vertical

6   distributions is limited as only elastic backscatter is analyzed and the signal to noise ratio of

7   space borne measurements is low. More opportunities for model validation are provided by

8   ground based multiwavelength Raman or HSRL systems. Such lidars by their nature have limited

9   spatial coverage but are better suited for characterization of the vertical distribution of particle

10   properties at a chosen location.

11   In our paper, we consider Raman lidar observations taken during a smoke/dust episode

12   over West Africa in December 2015 during the SHADOW campaign (Veselovskii et al., 2016),

13   and compare the vertical profiles of particle parameters with MERRA-2. The simultaneous

14   presence of dust and smoke layers in the atmosphere provides an opportunity to test the ability of

15   the model to reproduce the vertical structure of aerosol properties over the observation site.

17   **2. Measurement setup and data analysis**

18   **2.1   Observation site**

19   The observation site is located at the Institute for Research and Development (IRD)

20   Center, Mbour, Senegal (14^0N, 17^0W). Information about the SHADOW (study of SaHAran

21   Dust Over West Africa) campaign and instruments at the IRD site can be found in the recent

22   publication by Veselovskii et al. (2016). During the SHADOW campaign data from three lidar

23   instruments were available:

24   • Cimel CE-370 micropulse lidar (www.cimel.fr) operated 24 hours per day at 532 nm

25   allowing real-time monitoring of aerosol and cloud layers.

26   • Doppler lidar Windcube WLS 100 (www.leosphere.com) provided continuous

27   monitoring of the wind field in the range from 100 m to 5 km with 50 m range resolution.

28   • Multiwavelength Mie - Raman polarization lidar LILAS (LIlle Lidar AtmosphereS),

29   allowed simultaneous detection of elastic and Raman backscatter signals and thus provides

30   3β+2α observations along with depolarization ratio at 532 nm.

1   LILAS measurements were performed from inside a laboratory building through a

2   window at an angle of 47 deg with respect to the horizon. Acquiring Raman backscatter at 408

3   nm also permits profiling of the water vapor mixing ratio (WVMR) (Whiteman et al., 1992). For

4   calibration of the water vapor channel, radiosonde launches from Dakar (about 70 km away from

5   Mbour) were used. The large separation between the lidar and radiosonde locations prevented an

6   accurate calibration, so the WVMR data were used mainly to monitor the relative change of the

7   water vapor content. The temporal resolution of the measurements was approximately 3 minutes.

8   The backscattering coefficients and depolarization ratio were calculated with range resolution 7.5

9   m (with corresponding height resolution of 5.5 m). Resolution of extinction coefficient

10   measurements varied with height from 50 m (at 1000 m) to 125 m (at 7000 m).

11   Particle extinction (α) and backscattering (β) coefficients at 355 nm and 532 nm are

12   calculated from elastic and Raman backscatter signals, as described in Ansmann et al. (1992).

13   Backscattering coefficients at 1064 nm were calculated by the Klett method (Klett, 1981).

14   In the data analysis both volume (δ^v) and particle (δ) depolarization ratios are considered.

15   These ratios are defined as

$$\delta^v = \frac{\beta_{\perp}^{p} + \beta_{\perp}^{m}}{\beta_{\text{II}}^{p} + \beta_{\text{II}}^{m}} = C \frac{P_{\perp}}{P_{\text{II}}} \tag{1}$$

$$\delta = \frac{\beta_{\perp}^{p}}{\beta_{\text{II}}^{p}} \tag{2}$$

18   Here P is the power of the elastic backscatter signal. Superscripts "p" and "m" indicate particle

19   and molecule backscattering, while subscripts "⊥" and "II" indicate cross- and co-polarized

20   components, C is the calibration constant. Particle depolarization is calculated as suggested by

21   (Freudenthaler et al., 2009):

$$\delta = \frac{\left(1+\delta^{m}\right)\delta^{v} R - \left(1+\delta^{v}\right)\delta^{m}}{\left(1+\delta^{m}\right) R - \left(1+\delta^{v}\right)} \tag{3}$$

23   here δ^m is the molecular depolarization ratio and R is the aerosol scattering ratio:

$$R = \frac{\beta^{p} + \beta^{m}}{\beta^{m}} \tag{4}$$

1   For further convenience we will use notations $\beta = \beta_{II}^{p} + \beta_{\perp}^{p}$, and $\alpha = \alpha^{p}$. To characterize the

2   spectral dependence of β and α, the backscattering and extinction Ångström exponents (BAE and

3   EAE) for wavelengths λ_1 and λ_2 are calculated as:

$$A^{\beta} = \frac{\ln\left(\frac{\beta_{\lambda_1}}{\beta_{\lambda_2}}\right)}{\ln\left(\frac{\lambda_2}{\lambda_1}\right)}, \quad A^{\alpha} = \frac{\ln\left(\frac{\alpha_{\lambda_1}}{\alpha_{\lambda_2}}\right)}{\ln\left(\frac{\lambda_2}{\lambda_1}\right)} \tag{5}$$

2.2   MERRA-2 aerosol reanalysis

7   The MERRA-2 simulations of aerosol properties over the observation site were made

8   using the GOCART model (Chin et al. 2002) integrated within GEOS-5. The model includes

9   representations of dust, sea salt, black and organic carbon, and sulfate aerosols. The aerosol

10 components are assumed to be externally mixed. The optical properties of these aerosol

11 components are summarized in Appendix 1. Sulfate and carbonaceous aerosols are both assumed

12 to be in the fine mode. Sea salt and dust are both represented by five size bins spanning $0.1 - 10$

13 microns radius for dust and $0.03 - 10$ microns dry radius for sea salt, allowing for simulation of

14 both the fine and coarse fractions of each. A more complete description of how GOCART is

15 implemented in GEOS-5 is provided in Colarco et al. (2010), which also includes a detailed

16 evaluation of the model with respect to MODIS, MISR, and AERONET aerosol optical depth

17 observations.

18   Optical properties of the aerosols are primarily based on Mie calculations using the

19 particle properties as in Colarco et al. (2010) and Chin et al. (2002), with spectral refractive

20 indices from the Optical Properties of Aerosols and Clouds (OPAC, Hess et al. 1998) database.

21 However, for dust, non-spherical optical properties derived from an offline database are used

22 (Colarco et al. 2014). For sea salt, sulfate, and the hydrophilic portion of carbonaceous aerosol,

23 hygroscopic growth is considered following Chin et al. (2002), with growth factors from OPAC

24 and Gerber (1985). The refractive index for organic carbon is based on the 100% brown carbon

25 case from Hammer et al. (2016) and it is implemented as described in Colarco et al. (2017).

26   Sources of aerosols in the model include wind-speed based emissions of dust and sea salt,

27 fossil fuel combustion, biomass burning, biofuel consumption, biogenic particulate organic

28 matter, and oxidation of di-methyl sulfide (DMS) and SO_2, which includes volcanic sources.

Aerosol sinks include convective scavenging, dry deposition, and wet removal, where aerosol hygroscopic growth is considered in the calculation of particle fall velocity and deposition velocity. The model resolution is $0.5° \times 0.625°$ latitude by longitude with 72 hybrid-eta layers from the surface to 0.01 hPa. Additional details of the simulation can be found in Randles et al. (2017) and Buchard et al. (2017).

In MERRA-2, aerosol and meteorological observations are jointly assimilated within GEOS-5. Aerosols are assimilated by means of analysis splitting and the local displacement ensemble (LDE) methodology (Buchard et al. 2015, 2016). The system assimilated MODIS, AVHRR, MISR, and AERONET 550 nm AOD. AERONET measurements are interpolated to 550 nm using the Angström relationship and the closest available channels, generally 500 and 675 nm. The assimilation determines an AOD increment, which corrects the model AOD in a way that minimizes the differences between the model and observations. The AOD increment both corrects for misplaced aerosol plumes, and scales the aerosol mass mixing ratio to match the observations. The 2D AOD increment does not contain enough information to correct either the vertical distribution of aerosols or the aerosol composition. Thus, the model determines the aerosol speciation, optical properties, and vertical distributions, while the AOD increments modulate the aerosol mass. Thus, the assimilated aerosol distributions and physical and optical properties arise from the forecast model assumptions and the formulation of the aerosol data assimilation algorithm.

3. Results of the measurements

The smoke layers from forest fires near the equator were regularly observed over the instrumentation site during the wintertime measurement sessions made in December 2015 – January 2016. In our study we will focus on a strong smoke episode that occurred on 24-27 December 2015. The back trajectories for the air mass over Mbour on 25 December 2015 at 04:00 UTC are shown in fig.1 ether with map of fires on 20 December 2015 (https://worldview.earthdata.nasa.gov).

The air masses below 1500 m (red and blue lines) are transported over the desert and are strongly loaded by dust, while air masses at 3000 m (green line) arrive from the South and pass over the regions of forest fires, and thus can transport smoke particles. The Cimel MPL operated continuously through the period of 24-27 December and thus monitored the arrival and evolution

1   of the smoke layer, as shown in fig.2. An elevated smoke layer appears on 24 December around

2   00:00 UTC. The layer becomes thicker during the day but remains confined to the height interval

3   of 2.5 km– 4.0 km and stays well separated from the dust layer, which extends from the ground

4   to approximately 2.0 km. Such structure of the layers is preserved throughout 25 December, as

5   well.

6   Cirrus clouds appear at 08:00 UTC on 24 December at a height of 8 km, soon after the

7   smoke layer arrival (fig.2a) and persist throughout the smoke episode. After 12:00 UTC on 24

8   December the clouds start descending and by 7:00 UTC on 25 December the cloud base is below

9   6 km (fig.2b). On 26 December strong precipitation of ice particles occurs (fig.2c) and finally, on

10 27 December the cloud is located at the top of the smoke-dust layer (fig.2d).

11   Multiwavelength Raman lidar observations are available for the 23-25 December period

12 only. The height – temporal evolution of particle backscattering coefficient β_{532}, depolarization

13 ratio δ_{532} and water vapor mixing ratio w measured by Raman lidar on the nights 23-24 and 24-

14 25 December 2015 are shown in fig.3. Due to the geometrical overlap factor the extinction data

15 can be processed starting from approximately 750 m, thus plots of all parameters start at this

16 height. The depolarization ratios of pure dust observed during SHADOW are in the 30-35%

17 range (Veselovskii et al., 2016), while the depolarization ratio of smoke at 532 nm normally is

18 below 10% (e.g. Tesche et al., 2011, Burton et al., 2015). Hence depolarization measurements

19 provide a convenient way to separate the aerosols into dust and smoke components. On the night

20 of 23-24 December the dust layer extends up to 2500 m, but high depolarization ratio (>30%),

21 which is usually associated with pure dust, is observed only below 1000 m, meaning that in 1000

22 m – 2500 m range the dust is probably mixed with smoke. The optical depth of the elevated

23 smoke layer is rather small on 23-24 December (0.1 at 5:00 UTC), but on 24-25 December it

24 increases up to 0.25 making possible the calculation of extinction coefficients from the Raman

25 lidar signals. For analyzing the vertical distribution of smoke and dust particle parameters, we

26 focus on the nighttime measurements of 24-25 December 2015.

27   Fig.4 shows horizontal wind direction and speed measured by the wind lidar on 24-25

28 December. The range corrected signal of the wind lidar can be evaluated starting from 100 m

29 height, and the corresponding height – temporal image is shown in fig.5. The wind speed was

30 measured in the dust layer (< 1500 m) for the whole period, however inside the smoke layer the

31 backscatter signal is lower, so the measurements were possible only in the period of 16:00-22:00

UTC on 24 December. During 24-25 December 2015, the wind in the low troposphere (<1500 m) is mainly dominated by the easterly Harmattan continental trades. Deceleration and acceleration of the lower part of the Harmattan (<1000 m) are observed, respectively in the beginning of the afternoon and during the night. The vertical profile of the wind speed demonstrates the presence of a Low Level Jet (LLJ) where the maximum wind speed (Jet speed) is located at a height of 350 m (LLJ height) at 1:00 UTC. LLJs are known to contribute to regional horizontal aerosol transport and to increase vertical mixing. Indeed, the LLJ occurrence at 1:00 UTC increases the aerosol loading by transporting desert dust. The corresponding increase of backscattering due to the LLJ at 1:00 UTC on 25 December can also be seen in fig.5.

Vertical profiles of temperature T, potential temperature Θ, wind direction and speed together with relative humidity RH and water vapor mixing ratio (WVMR) from radiosonde launched from Dakar at 00:00 UTC on 25 December 2015 are shown in fig.6. The profile of wind speed and wind direction obtained from the sonde confirms that the LLJ observed with lidar at Mbour is not a local phenomenon, because it is also observed at Dakar. The vertical profile of potential temperature suggests that the Nocturnal Boundary Layer (NBL) top corresponds to the LLJ height. Above 3000 m, the lidar and sonde depict southerly winds which transport the smoke plume. Water vapor mixing ratio increases above 2500 m; as a result the RH in the smoke layer reaches 75% while in the dust layer RH is below 30%.

To quantify the vertical distribution of particle parameters, fig.7 shows profiles of backscattering (β_{355}, β_{532}, β_{1064}) and extinction (α_{355}, α_{532}) coefficients derived from Raman lidar measurements for three temporal intervals on the night of 24-25 December: 19:00-23:00 UTC, 1:00-4:00 UTC and 4:00-7:00 UTC. The particle depolarization ratios δ_{532} for the same intervals together with the water vapor mixing ratio w are shown in fig.8, while extinction and backscattering Ångström exponents $A^{\alpha}_{355/532}$, $A^{\beta}_{355/532}$, $A^{\beta}_{532/1064}$ are given by fig.9. For the first temporal interval (fig.7a) dust and smoke layers are well separated. Extinction coefficients α_{355} and α_{532} differ in the smoke layer ($\alpha_{355}>\alpha_{532}$), but inside the near-surface dust layer (below 1750 m) the extinction values are nearly the same. The depolarization ratio is δ_{532}=35±5% at 750 m and it gradually decreases with height to 27±4% at 1750 m. Above that height δ_{532} decreases quickly, indicating an increase in the contribution of smoke particles. For the second and third temporal intervals the dust and smoke layers appear to mix leading to layering in the

1   backscattering coefficient in the 1000 m − 2000 m range. The EAE in this range is increased up

2   to 0.5 (fig.9c) indicating that these layers may contain significant amounts of smoke.

3   The EAE of pure dust observed during SHADOW is slightly negative $A^{\alpha}_{355/532} \approx -0.1$

4   (Veselovskii et al., 2016). In fig.9a the EAE below 1500 m is about 0.2±0.2, so the dust likely

5   contains some amount of smoke. Values of EAE close to zero are observed in fig.9a,c below

6   1000, where the depolarization ratio increases up to 35±5%. Inside the dust layer $\beta_{355}<\beta_{532}$, so

7   the corresponding backscattering Ångström exponent is negative. The negative values of $A^{\beta}_{355/532}$

8   have been already reported by Veselovskii et al., (2016), where negative BAE was attributed to

9   an increase of the imaginary part of the complex refractive index at 355 nm compared to 532 nm.

10   In the center of the elevated layer at 3100 m $\delta_{532}=14\pm3\%$, while at the top of this layer δ_{532}

11   decreases to 6±1.5% (fig.8a), indicating a possible presence of dust particles in the center of

12   elevated layer. The loading of elevated layer with dust particles is supported also by the profiles

13   of $A^{\beta}_{355/532}$: for all three temporal intervals $A^{\beta}_{355/532}$ demonstrates the dip in the center of elevated

14   layer, while $A^{\alpha}_{355/532}$ and $A^{\beta}_{532/1064}$ do not decrease in 2500- 4000 m range. As mentioned, for pure

15   dust $A^{\beta}_{355/532}$ is negative, so presence of dust in the center of smoke layer should decrease the

16   backscattering Ångström exponent. The presence of dust in the smoke layer is not surprising,

17   because upwelling airflows in forest fires region can lift a significant amount of dust together

18   with biomass burning products.

19   Profiles of lidar ratios at 355 nm and 532 nm, for the same temporal intervals as in fig.7,

20   are shown in fig.10. Lidar ratios in the dust layer at 532 nm and 355 nm for 19:00-23:00 UTC

21   period are $LR_{532}=55\pm8$ sr and $LR_{355}=70\pm10$ sr, respectively. At the top of the elevated layer,

22   where the smoke particles are predominant, the lidar ratios for the same period are higher:

23    $LR_{532}=65\pm10$ sr and $LR_{355}=75\pm11$ sr. Due to the presence of dust in the center of the elevated

24   layer, the height dependence of lidar ratios shows a decrease, with a minimum at approximately

25   3000 m for all three temporal intervals. The decrease is more pronounced at 532 nm, because the

26   difference between smoke and dust lidar ratios is larger at this wavelength. The lidar ratios below

27   2000 m at 01:00-04:00 and 04:00-07:00 UTC become strongly oscillating because of high

28   gradients of backscattering and extinction coefficients at low altitudes and are not shown due to

29   high uncertainties.

1   Fig.11, shows the dependence of the particle depolarization ratio δ_{532} on the extinction

2   Ångström exponent derived from data in fig.7 a. The depolarization ratio monotonically

3   decreases while EAE rises from 0 to 0.9. The observed high values of the depolarization ratio

4   are attributed to big dust particles with EAE close to zero, while small smoke particles are

5   characterized by low depolarization (below 10%). If depolarization ratios of smoke δ^s and dust δ^d

6   are known, the contributions of smoke and dust particles to the total backscattering can be

7   separated $\beta = \beta^s + \beta^d$ (Sugimoto and Lee, 2006; Tesche et al., 2009; Miffre et al., 2012; David

8   et al., 2013, Burton et al., 2014). Assuming that depolarization ratios of dust and smoke particles

9   do not change with height the contributions β^d and β^s can be calculated as suggested by Tesche et

10 al. (2009):

11   $$\beta^d = \beta \frac{(\delta - \delta^s)}{(\delta^d - \delta^s)} \frac{(1 + \delta^d)}{(1 + \delta)} \text{ and } \beta^s = \beta - \beta^d ,$$ (6)

12 In our computations we used values $\delta^d = 35\%$ and $\delta^s = 7\%$.

13   The results of the decomposition of β_{532} for β_{532}^d and β_{532}^s components for the same three

14 temporal intervals as in fig.7 are shown in fig.12. This figure presents total backscattering

15 coefficient β_{532} together with particle depolarization ratio δ_{532}. The dust contribution to

16 backscattering is marked with magenta, while residual backscattering $\beta_{532} - \beta_{532}^d$ is attributed to

17 the smoke and is marked with grey. For the height regions with low backscattering the

18 uncertainty of β_{532} is high, so the decomposition for these regions is not shown. The dust is

19 predominant below 1700 m for 19:00-23:00 UTC period, however even the elevated layer

20 contains a significant amount of dust: at 3100 m $\beta_{532}^d \approx 0.3\beta_{532}$. After 01:00 UTC the smoke

21 layers descend (fig and their contribution to backscattering becomes significant down to 1000

22 m height. We should recall that though lidars were widely used for the study of smoke layers

23 over Europe and United States (e.g. Amiridis et al., 2009; Nicolae et al., 2015; Burton et al.,

24 2015; Veselovskii et al., 2015) the contribution of dust to the smoke layers properties was

25 normally not considered. However, the contribution of dust may become important since dust

26 particles in Africa can be lifted during the forest fire and transported over large distances.

28   **4**. **Comparison of lidar measurements with MERRA-2**

1   MERRA-2 provides vertical distribution of mass mixing ratios of five aerosol

2   components, so for each of these components the extinction, backscattering coefficients and

3   depolarization ratios can be calculated. Vertical profiles of extinction coefficient of dust, black

4   carbon (BC), organic carbon (OC), sea salt (SS) and sulfates (SU) together with total extinction

5   α_{532} are shown in fig.13 for 03:00 UTC and 21:00 UTC on 24 December 2015. At 03:00 UTC

6   the aerosol is localized below 3000 m. Dust extinction is predominant, but contribution of OC to

7   the total extinction coefficient rises with height reaching maxima at 2250 m. The presence of a

8   significant amount of OC agrees with the low values of depolarization ratio above 1500 m for

9   this temporal interval in fig.3.

10   At 21:00 UTC an elevated layer with a maximum of extinction at 3150 m is observed

11   (fig.13b). In this layer OC and dust provide similar contributions to extinction (about 40% at

12   3150 m height). From the results shown in fig.12a we can estimate the contribution of dust to

13   α_{532} in the center of elevated layer as 30% (by assuming the dust lidar ratio $LR_{532}=55$ sr), so the

14   measured and simulated dust contributions are in good agreement. Below 1750 m the dust is the

15   main contributor to the extinction coefficient providing 88% of α_{532} at 1000 m (fig.13b). The

16   observed dust contribution to α_{532} at the same height is about 90% (fig.12a), which again shows

17   good agreement between the model and measurements. Total contribution of BC and SU to

18   extinction is below 20% in the elevated smoke layer, and in the near-surface dust layer their

19   contribution is negligible. The extinction coefficients can be recalculated to the backscattering

20   using model lidar ratios of the aerosol components. Fig.13c shows the profiles of backscattering

21   coefficients at 532 nm computed for the same temporal interval as in Fig.13b. The simulation of

22   the backscattering coefficient is more challenging than that of extinction, because backscatter

23   depends more strongly on the particle morphology and refractive index. A detailed comparison

24   of measured and modeled profiles of backscattering coefficients will be performed later in this

25   section.

26   As mentioned, the comparison of model and observed values is more straightforward for

27   extinction coefficients. Fig.14 shows the time-series of extinction profiles at 355 nm and 532 nm

28   modeled for the night of 24-25 December 2015 at 18:00, 21:00, 00:00, 03:00, 06:00 UTC. The

29   profiles are shifted relative to each other on 0.1 km^{-1}. The corresponding profiles of extinction

30   coefficients measured by Raman lidar are shown in fig.15. For convenience of comparison,

31   fig.16 presents measured and modeled α_{355} profiles from fig.14 and fig.15 now plotted together.

1 The model reproduces well the location of the elevated smoke layer, as well as the top of the

2 near-surface dust layer. However, the model does not resolve the oscillations of extinction

3 profile below 2000 m at 03:00 and 06:00 UTC on 25 January.

4   To quantify the difference between measured (α_{355}^{meas}) and modeled (α_{355}^{mod}) extinction

5 coefficients at 355 nm, fig.17 shows profiles of extinctions difference $\Delta\alpha_{355} = \alpha_{355}^{meas} - \alpha_{355}^{mod}$ for

6 results from fig.16. The difference is normally below 0.1 km^{-1}. The frequency distribution of

7 $\Delta\alpha_{355}$ for all five profiles is shown in fig.18. The mean value is -0.01 km^{-1} with standard

8 deviation of 0.042 km^{-1}. With typical values of extinction coefficient in elevated smoke layer and

9 near-surface dust layer being on the order of 0.2 km^{-1}, the relative difference of modeled and

10 measured extinction is estimated to be below 25% for the time period considered.

11   To analyze how well the model reproduces the temporal variations of aerosol optical

12 depth, fig.19 presents AODs at 355 nm on 23 – 24 December 2015 for two height intervals: 750

13 m – 2000 m and 2500 m – 4500 m. The first interval corresponds to the near-surface dust layer,

14 while the second interval corresponds to the elevated smoke layer. The AOD is calculated from

15 the Raman backscatter, and in the day time measurements could be processed only in the dust

16 layer, due to enhanced background noise. Thus day time measurements in the elevated smoke

17 layer are not plotted. The time of the appearance of the smoke layer is well represented in the

18 model results (about 00:00 UTC on 24 December), however the lidar derived AOD of this layer

19 increases rapidly from the first appearance of the layer, while in the model the rapid increase in

20 AOD growth starts approximately 5 hours later. The model predicts that the maximum value of

21 AOD in the smoke layer (0.27) is reached at 20:00-24:00 UTC interval, which reasonably agrees

22 with observations: mean value of measured AOD for this interval is 0.23±0.02. After midnight

23 the modeled AOD of the smoke layer decreases quickly, while lidar measured AOD stays about

24 0.25. The measured AOD of the near-surface layer agrees with the model. The observed AOD

25 exceeds the model values in the beginning (at 00:00 UTC on 24 December measured and

26 modeled AODs are 0.24 and 0.175, respectively), but after 10:00 UTC, the values are in better

27 agreement. Thus, we can conclude that the model reproduces the temporal variability of AOD in

28 the dust and smoke layers.

29   The agreement between modeled and observed extinction profiles provides an

30 opportunity to test how well the backscattering coefficients can be modeled. Simulation of

31 backscattering coefficients is especially challenging for dust for several reasons. First of all, we

1   are not confident in the accuracy of the presumed scattering phase function in the backward

2   direction. Second, the backscattering coefficient strongly depends on the particle refractive

3   index, in particular on the imaginary part, which may vary over a wide range depending on dust

4   origin. The in situ ground measurements in West Africa, performed during the SAMUM field

5   campaign, demonstrate that the mean value of m_I for dust episodes is about 0.003 at 532 nm and

6   0.02 at 355 nm. However deviation from these mean values for every individual measurement

7   can be significant (Müller et al., 2009; Kandler et al., 2011; Ansmann et al., 2011). The

8   imaginary part of RI of dust in the model is assumed to be 0.007 at 355 nm, following previous

9   OMI data analysis (Torres et al., 2007) and 0.0025 at 532 nm.

10   Fig.20 shows measured and modeled backscattering coefficients at 355 nm and 532 nm

11   for the same five temporal intervals as in fig.16. At 355 nm the modeled and measured values

12   agree for both the smoke and dust layers. However at 532 nm the backscattering coefficients

13   agree only inside elevated layer, while below 1750 m the modeled β_{532} significantly exceeds the

14   measured values. As mentioned, the modeled lidar ratio LR_{532} for the mixture is close to 40 sr at

15   1000 m, while the measured lidar ratio in the near surface dust layer is 55±8 sr. The reason for

16   this disagreement could be that the assumed imaginary part of the refractive index for dust

17   (0.0025 at 532 nm) is too low. Recall however, that we cannot determine the imaginary part of

18   the refractive index for dust by simply adjusting the modeled lidar ratio to the measured one,

19   because the lidar ratio depends on several factors besides m_I such as the particle size distribution

20   and the aspect ratio of the ellipsoids used in the model. It is possible that the particle size

21   distribution in the model is too much weighted toward fine mode dust.

22   The modeled and measured particle intensive parameters, such as extinction $A^{\alpha}_{355-532}$ and

23   backscattering $A^{\beta}_{355-532}$ Ångström exponents together with the particle depolarization ratio δ_{532}

24   are shown in fig.21. The measurements are averaged over 19:00 − 23:00 UTC interval while

25   modeled values are given for 21:00 UTC. The model reproduces well the observed vertical

26   distribution of $A^{\alpha}_{355-532}$ both in the dust and the elevated layer. As follows from fig.7a, inside the

27   dust layer $\beta_{355} < \beta_{532}$, so the corresponding $A^{\beta}_{355-532}$ is negative with a minimum value of about -

28   0.4. The model predicts values of $A^{\beta}_{355-532}$ as low as -1.4. The modeled BAE is sensitive to the

29   choice of the imaginary part of RI at 355 nm and 532 nm and, as mentioned, the chosen

30    $m_I(532)=0.0025$ may be too low for this episode. In the elevated layer the modeled $A^{\beta}_{355-532}$ is

1   close to the observed one. The modeled BAE has no minimum in the center of elevated layer,

2   because the modeled ratio of dust and OC aerosol concentrations shows only a small variation

3   throughout the elevated layer.

4   The model reproduces reasonably well the depolarization in the elevated layer, but inside

5   the dust layer the modeled δ_{532} is significantly lower than what is observed (22% compared to

6   35%). This problem is well known: the spheroidal model underestimates the depolarization ratio

7   when typical dust PSD and complex refractive index are used (Veselovskii et al., 2010; Wiegner

8   et al., 2009; Müller et al., 2013; Nowottnick et al., 2015).

9   One of the MERRA-2 data products is the water vapor mixing ratio (WVMR), which

10   helps to identify atmospheric parcels, is critically important for determining atmospheric stability

11   and serves as the source of water for aerosol hygroscopic growth. Fig.22 shows five model

12   profiles of WVMR together with the results of Raman lidar measurements for the same temporal

13   intervals as in fig.14. The model reproduces rather well the WVMR profile inside the elevated

14   layer (2500 m – 4500 m) on 24 December, though on 25 December the modeled values in this

15   range are lower than the observations. In the near-surface dust layer, the deviation of modeled

16   values from the measurements is larger. Statistical analysis of the deviation of modeled values

17   from lidar measurements for all five profiles (the same as in fig.18), shows that mean difference

18   is 0.04 g/kg with standard deviation of differences of 1.6 g/kg. Thus in the elevated layer, where

19   WVMR is approximately 8 g/kg, the agreement is quite good, however in the dust layer, which is

20   characterized by low water vapor content (below 4 g/kg), the difference may be up to 40%.

22   **5. Inversion of lidar measurements to particle microphysical properties**

23   In the previous section, as validation of the model output we compared the modeled

24   aerosol optical parameters, such as extinction, backscattering coefficients, and depolarization

25   ratio with the values derived from lidar measurements in a straightforward way. The comparison

26   of particle microphysical properties such as volume, effective radius and complex refractive

27   index, however, is not straightforward, since it needs inversion of the measurements and requires

28   additional assumptions. In the case of dust particles the inversion becomes especially

29   challenging, because:

30   -   The size distribution of dust contains a strong coarse mode with particle radii

31   extending up to ~ 15 μm, and the estimation of properties for such big particles is

1   difficult since measurements are only performed in the wavelength range 0.355-1.064

2   μm;

3   -   The inversions have to consider the refractive index as spectrally independent. In fact,

4    the imaginary part of the dust RI is spectrally dependent with a strong enhancement at

5    355 nm compared to 532 nm;

6   -   The dust particles are not spherical so that the application of Mie formulas for the

7    forward modeling results in errors in computing the scattering phase function.

8   Regarding shape issue, one of the ways to mimic the scattering properties of dust

9 particles is to use the model of randomly oriented spheroids (Mishchenko et al., 1997; Dubovik

10 et al., 2006). The implementation of this model for inversion of dust lidar measurements is

11 described in Veselovskii et al., (2010, 2016), and Müller et al., (2013). This algorithm was used

12 also for inversion of our 3β+2α observations. The range of particle radius in the inversion has

13 been set to a minimum and maximum of 0.075 and 15 μm, respectively. The real part of RI was

14 allowed to vary in the range 1.35 - 1.65, while the imaginary part varied in the range 0 - 0.02.

15 The refractive index was assumed to be spectrally independent. The effects of a possible spectral

16 dependence of the imaginary part of RI were considered in Veselovskii et al., (2016).

17   Profiles of the effective radius, volume density, and real part of the refractive index

18 retrieved from optical measurements in fig.7a are shown in fig.23. The inversion was performed

19 for two cases, with the assumption of all spherical particles (SVF=0) or all spheroids

20 (SVF=100%). A realistic solution (for the mixture of spherical and non-spherical particles),

21 should be closer to spheroids in the dust layer, while in the elevated layer it should be closer to

22 the results obtained with spheres. The model results provided by MERRA-2 are shown on the

23 same plot. The effective radius and volume density obtained in assumption of spherical particles

24 are always higher than the values obtained with spheroids. The modeled effective radius at 1000

25 m height is 1.1 μm, which is close to r_{eff}=1.0±0.3 μm obtained from lidar measurements using

26 the spheroids model. Lidar derived effective radius in the elevated layer at 3000 m is

27 approximately 0.4 μm and 0.5 μm when spheroids and spheres are used respectively, while the

28 modeled value is 0.3 μm. The reason for the lower value of modeled effective radius is the

29 contribution of black carbon, which is characterized by small size and relatively low hygroscopic

30 growth. Recall that in the inversion of lidar measurements, the smallest radius considered is

1   0.075 μm. Modeled values of the volume density agree well with lidar retrievals in both dust and

2   elevated layers.

3   The estimation of the real part of RI from lidar measurements is sensitive to the type of

4   kernel functions chosen for retrieval. In the regularization algorithm the treatment of dust

5   particles as spheres strongly underestimates m_R (Veselovskii et al., 2010), so results obtained

6   with spheres in the dust layer are not shown in fig.23c. At 1000 m the m_R retrieved with

7   spheroids is 1.52±0.05, which agrees well with the modeled value. Inside the elevated smoke

8   layer, where fine mode particles predominate, the application of spheroids overestimates m_R. The

9   lidar derived real part of RI at 3000 m is 1.43±0.05 for spheres and 1.51±0.05 for spheroids, so

10   we expect that the true value would lie within this. The simulated value of m_R=1.50 in the

11   elevated layer is quite high, which is again the result of BC contribution.

12   The single scattering albedo (SSA) is one of the key parameters to be retrieved and

13   conclusions about the potential of the multiwavelength lidar method strongly rely on its ability to

14   profile SSA. Fig.24 shows SSA at 355 nm, 532 nm and 1064 nm. As mentioned, the spectral

15   dependence of m_I was not accounted for and the algorithm retrieves an average value of the

16   imaginary part over the interval of 355 nm – 1064 nm. In particular, for dust and OC the

17   imaginary part is underestimated at 355 nm and overestimated at 532nm and 1064 nm. As a

18   result, in the dust layer the retrieved SSA exceeds the model values at 355 nm, while at 532nm

19   and 1064 the situation is opposite. Still at a height of 1000 m, the difference between modeled

20   and lidar derived SSAs is below 0.04 for all wavelengths. In the elevated layer, where the

21   spectral dependence of m_I is less pronounced, the simulated and retrieved SSA agree well with a

22   corresponding difference of less than 0.02.

24   **6. Summary and conclusion**

25   In our study we have considered a smoke/dust episode over West Africa to compare the

26   vertical profiles of particle parameters modeled by MERRA-2 and retrieved from Raman lidar

27   measurements. The Raman lidar provides profiles of backscattering and extinction coefficients at

28   355 nm and 532 nm with uncertainty below 10%, so comparison of these parameters with model

29   predictions can be considered as a type validation. In the case we selected, the simultaneous

30   presence of the dust and smoke layers resulted in significant height variation of particle

1   parameters, providing a good opportunity to test the models' capability to reproduce complicated

2   vertical structure.

3   Modeled and observed vertical profiles of α_{355} and α_{532} show good similarity: MERRA-2

4   provides the correct location of both the near-surface and elevated layers. The mean difference

5   between modeled and observed extinction coefficients for profiles considered is approximately

6   0.01 km^{-1} with standard deviation of 0.042 km^{-1}. Good coherence between measured and

7   modeled extinction provides an opportunity to test, how well the model reproduces particle

8   backscattering. One of the issues in such a comparison is the spectral dependence of the

9   imaginary part of the refractive index of dust. The m_I can change significantly for dust of

10   different origin and this variability may be accounted for in future model developments. Still

11   even for the current version, comparisons of modeled and measured β_{355} show good agreement in

12   the dust layer At 532 nm however, the modeled backscattering coefficients in the dust layer

13   exceed the observed values. The modeled lidar ratio is about 40 sr, while the measured LR_{532} in

14   the dust layer is about 55 sr. This discrepancy may be an indication that m_I of dust during the

15   episode considered is higher than the value assumed in the model. Another possible explanation

16   is that the model particle size distribution is too much weighted toward fine mode dust. The

17   backscattering coefficients inside the smoke layer agree with modeled values for both 355 nm

18   and 532 nm wavelengths. The measured lidar ratios at the top of the elevated layer, where smoke

19   particles are predominant, are $LR_{355}=75\pm11$ sr and $LR_{532}=70\pm10$ sr, which is close to the

20   corresponding model values for organic carbon of 71 sr and 66 sr, respectively.

21   MERRA-2 predicts the existence of a significant amount of dust in the elevated smoke

22   layer, and the high values of observed depolarization ratio agree with this prediction. The

23   existence of minima of $A^{\beta}_{355/532}$ in the center of elevated layer, characterized by the highest δ_{532}

24   also supports this finding. Moreover, the lidar ratios at both 355 and 532 nm also have a minima

25   in the center of the layer because the lidar ratio of dust is lower than that of smoke. The

26   contributions of dust and smoke particles to the backscattering and extinction coefficient at 532

27   nm evaluated from particle depolarization ratio agree with the values provided by the model. We

28   should recall that in lidar studies of forest fire smoke variation of the depolarization ratio

29   throughout the smoke plume is usually related to the aging processes in the plume. However, we

30   should also consider the possibility that there may be mineral dust present in the plume, and

31   MERRA-2 modeling can be helpful for such an analysis.

1   Analysis of only one episode is not sufficient for broad conclusions regarding how well

2   the model reproduces the vertical distribution of particle properties. More measurements at

3   different locations are needed. However, the results presented here demonstrate the potential of

4   synergy between the model and lidar measurements. Analysis of different measurement sessions

5   along with the use of modeled particle parameters in lidar retrieval schemes are in our future

6   plans.

8   Acknowledgments: The authors are very grateful to IRD-Dakar (Institut de Recherche pour le

9   Développement) for their welcome and efficient support and also thank the labex CaPPA for

10   supporting this campaign. The CaPPA project (Chemical and Physical Properties of the

11   Atmosphere) is funded by the French National Research Agency (ANR) through the PIA

12   (Programme d'Investissement d'Avenir) under contract "ANR-11-LABX-0005-01" and by the

13   Regional Council" Nord-Pas de Calais » and the "European Funds for Regional Economic

14   Development (FEDER). Development of lidar retrieval algorithms was supported by Russian

15   Science Foundation, (project 16-17-10241).

1 **References**

2 Alexandrov, M. and Mishchenko, M.: Information content of bistatic lidar observations of
3   aerosols from space, Opt. Expr. 25, 134-150, 2017.

4 Amiridis, V., Balis, D. S., Giannakaki, E. , Stohl, A., Kazadzis, S., Koukouli, M. E., and Zanis,
5   P.: Optical characteristics of biomass burning aerosols over southeastern Europe determined
6   from UV–Raman lidar measurements, Atmos. Chem. Phys., 9, 2431–2440, 2009.

7 Ansmann, A., Wandinger, U., Riebesell, M., Weitkamp, C.and Michaelis,W., "Independent
8   measurement of extinction and backscatter profiles in cirrus clouds by using a combined
9   Raman elastic-backscatter lidar", Appl. Opt. 31, 7113–7131, 1992.

10 Ansmann, A., Petzold, A., Kandler, K., Tegen, I., Wendisch, M., Müller, D., Weinzierl, B.,
11   Müller, T., Heintzenberg, J.: Saharan Mineral Dust Experiments SAMUM–1 and SAMUM–
12   2: what have we learned?, Tellus, 63B, 403–429, 2011.

13 Böckmann, C., Miranova, I., Müller, D., Scheidenbach, L., Nessler, R.: "Microphysical aerosol
14   parameters from multiwavelength lidar," J. Opt.Soc. Am. A 22, 518–528, 2005.

15 Buchard, V., Randles, C.A., Da Silva, A.M., Darmenov, A., Colarco, P.R., Govindaraju, R.,
16   Ferrare, R., Hair, J., Beyersdorf, A.J., Ziemba, L.D., and Yu, H.: The MERRA-2 Aerosol
17   Reanalysis, 1980 Onward. Part II: Evaluation and Case Studies, Journal of Climate, 30,
18   6851-6872, 2017.

19 Burton, S. P., Vaughan, M. A., Ferrare, R. A. and Hostetler, C. A.: Separating mixtures of
20   aerosol types in airborne High Spectral Resolution Lidar data. Atmos. Meas. Tech., 7, 419–
21   436, 2014.

22 Burton, S. P., Hair, J. W., Kahnert, M., Ferrare, R. A., Hostetler, C. A., Cook, A. L., Harper, D.
23   B., Berkoff, T. A., Seaman, S. T., Collins, J. E., Fenn, M. A., and Rogers, R. R.:
24   Observations of the spectral dependence of linear particle depolarization ratio of aerosols
25   using NASA Langley airborne high spectral resolution lidar, Atmos. Chem. Phys. 15, 13453–
26   13473, 2015.

27 Burton, S. P., Chemyakin, E., Liu, X., Knobelspiesse, K., Stamnes, S., Sawamura, P., Moore, R.
28   H., Hostetler, C. A., and Ferrare, R. A.: Information content and sensitivity of the $3\beta+2\alpha$
29   lidar measurement system for aerosol microphysical retrievals, Atmos.Meas. Tech., 9, 5555–
30   5574, 2016.

1 Chemyakin, E., Müller, D., Burton, S., Kolgotin, A., Hostetler, C., Ferrare, R.: "Arrange and
2   average algorithm for the retrieval of aerosols parameters from multiwavelength
3   HSRL/Raman lidar data," Appl. Opt. 53, 7252–7266, 2014.
4 Chin, M., Ginoux, P., Kinne, S., Torres, O., Holben, B., Duncan, B., Martin, R.V., Logan, J.A.,
5   Higurashi, A., Nakajima, T.: Tropospheric aerosol optical thickness from the GOCART
6   model and comparisons with satellite and Sun photometer measurements, Journal of the
7   Atmospheric Sciences, 59, 461–483, 2002.
8 Colarco, P., Da Silva, A., Chin, M., and Diehl, T.: Online simulations of global aerosol
9   distributions in the NASA GEOS-4 model and comparisons to satellite and ground-based
10   aerosol optical depth. Journal of Geophysical Research 115, doi.10.1029/2009JD012820,
11   2010.
12 Colarco, P. R., Nowottnick, E. P., Randles, C. A., Yi, B., Yang, P., Kim, K.-M., Smith, J. and
13   Bardeen, C.G.: Impact of radiatively interactive dust aerosols in the NASA GEOS-5 climate
14   model: Sensitivity to dust particle shape and refractive index. Journal of Geophysical
15   Research-Atmospheres, 119(2), 753–786,. doi.10.1002/2013JD020046, 2014.
16 Colarco, P. R., Gasso', S., Ahn, C., Buchard, V., da Silva, A. M. and Torres, O.: Simulation of
17   the Ozone Monitoring Instrument Aerosol Index using the NASA Goddard Earth Observing
18   System Aerosol Reanalysis Products, Atmos. Meas. Tech. Discuss., 1–22, doi:10.5194/amt-
19   2017-87, 2017.
20 David, G., Thomas, B., Nousiainen, T., Miffre, A., and Rairoux, P.: Retrieving simulated
21   volcanic, desert dust and sea-salt particle properties from two/three-component particle
22   mixtures using UV-VIS polarization lidar and T matrix, Atmos. Chem. Phys., 13, 6757–
23   6776, 2013.
24 Dubovik, O., Sinyuk, A., Lapyonok, T., Holben, B.N., Mishchenko, M., Yang, P., Eck, T.F.,
25   Volten, H., Munoz, O., Veihelmann, B., van der Zande, W.J., Leon, J.-F., Sorokin, M.,
26   Slutsker, I.: Application of spheroid models to account for aerosol particle nonsphericity in
27   remote sensing of desert dust, *J. Geophys. Res*., 111, D11208, doi:10.1029/2005JD006619,
28   2006.
29 Freudenthaler,V., Esselborn, M.,Wiegner, M.,Heese, B., Tesche, M. and co-authors:
30   Depolarization ratio profiling at severalwavelengths in pure Saharan dust during SAMUM
31   2006, *Tellus* 61B, 165–179, 2009.

2   Gelaro, R., McCarty, W., Suarez, M.J., Todling, R., Molod, A., Takacs, L., Randles, C.A.,

3   Darmenov, A., Bosilovich, M.G., Reichle, R., Wargan, K., Coy, L., Cullather, R., Draper,

4   C., Akella, S., Buchard, V., Conaty, A., Da Silva, A.M., Gu, W., Kim, G.K., Koster, R.,

5   Lucchesi, R., Merkova, D., Nielsen, J.E., Partyka, G., Pawson, S., Putman, W., Rienecker,

6   M., Schubert, S.D., Sienkiewicz, M., and Zhao, B.: The Modern-Era Retrospective Analysis

7   for Research and Applications, Version 2 (MERRA-2), Journal of Climate, 30, 5419-5454

8   2017.

9   Gerber, H. E., 1985: Relative-humidity parameterization of the Navy Aerosol Model (NAM).

10   Tech. Rep. NTIS ADA1632090, Naval Research Laboratory, Washington, DC.

11 Hammer, M. S., Martin, R. V., van Donkelaar, A., Buchard, V., Torres, O., Ridley, D. A. and

12   Spurr, R. J. D.: Interpreting the ultraviolet aerosol index observed with the OMI satellite

13   instrument to understand absorption by organic aerosols: implications for atmospheric

14   oxidation and direct radiative effects, Atmos Chem Phys, 16, 2507–2523, 2016.

15 Hess, M., Koepke, P., and Schult, I.: Optical properties of aerosols and clouds: The software

16   package OPAC, Bulletin of the American Meteorological Society, 79, 831–844, 1998.

17 Kahnert, M. and Andersson, E: How much information do extinction and backscattering

18   measurements contain about the chemical composition of atmospheric aerosol? Atmos.

19   Chem. Phys., 17, 3423–3444, 2017.

20 Kandler, K., Lieke, K., Benker, N., Emmel, C., Küpper, M., Müller-Ebert,D., Ebert, M.,

21   Scheuvens, D., Schladitz, A., Schütz, L., Weinbruch, S.: Electron microscopy of particles

22   collected at Praia, Cape Verde, during the Saharan Mineral Dust Experiment: Particle

23   chemistry, shape, mixing state and complex refractive index. Tellus 63B, 475-496, 2011.

24 Klett, J. D.: Stable analytical inversion solution for processing lidar returns, Appl. Opt. **20,** 211–

25   220, 1981.

26 Kolgotin, A., Müller, D., Chemyakin, E., Romanov, A.: "Improved identification of the solution

27   space of aerosol microphysical properties derived from the inversion of profiles of lidar

28   optical data, part 1: theory," Appl. Opt. 55, 9839–9849, 2016.

29 Miffre, A., David, G., Thomas, B., Rairoux, P., M. Fjaeraa, A., Kristiansen, N.I., Stohl, A.:

30   Volcanic aerosol optical properties and phase partitioning behavior after long-range

1 advection characterized by UV-Lidar measurements, Atmospheric Environment 48, 76-84,
2   2012.
3 Mishchenko, M.I., L.D. Travis, R.A. Kahn, and R.A. West, Modeling phase functions for
4   dustlike tropospheric aerosols using a mixture of randomly oriented polydisperse spheroids,
5   J. Geophys. Res., Vol. 102, 16831-16847, 1997
6 Müller, D., Wandinger, U., and Ansmann, A.: Microphysical particle parameters from extinction
7   and backscatter lidar data by inversion with regularization: theory, Appl. Opt. 38, 2346-2357,
8   1999.
9 Müller, D., Mattis, I., Wandinger, U., Ansmann, A., Althausen, D., Stohl, A.: Raman lidar
10   observations of aged Siberian and Canadian forest fire smoke in the free troposphere over
11   Germany in 2003: Microphysical particle characterization, J. Geophys. Res., 110, D17201,
12   doi:10.1029/2004JD005756, 2005.
13 Müller, D., Veselovskii, I., Kolgotin, A., Tesche, M., Ansmann, A., Dubovik, O.: Vertical
14   profiles of pure dust (SAMUM-1) and mixed smoke-dust plumes (SAMUM-2) inferred from
15   inversion of multiwavelength Raman/polarization lidar data and comparison to AERONET
16   retrievals and in-situ observations, Appl.Opt. 52, 3178-3202, 2013.
17 Müller, D., Böckmann, C., Kolgotin, A., Schneidenbacha, L., Chemyakin, E., Rosemann, J.,
18   Znak, P., and Romanov, A.: Microphysical particle properties derived from inversion
19   algorithms developed in the framework of EARLINET, Atmos. Meas. Tech., 9, 5007–5035,
20   2016.
21 Müller, T., Schladitz, A., Massling, A., Kaaden, N., Kandler, K. and Wiedensohler A.: Spectral
22   absorption coefficients and imaginary parts of refractive indices of Saharan dust during
23   SAMUM-1, Tellus 61B, 79–95, 2009.
24 Nicolae D., A. Nemuc, D. Müller, C. Talianu, J. Vasilescu, L. Belegante, and A. Kolgotin:
25   Characterization of fresh and aged biomass burning events using multi-wavelength Raman
26   lidar and mass spectrometry, J. Geophys. Res. 118, 2956–2965, doi:10.1002/jgrd.50324,
27   2013.
28 Nowottnick, E. P., Colarco, P. R., Welton, E. J., da Silva, A.: Use of the CALIOP vertical feature
29   mask for evaluating global aerosol models, Atm. Meas. Tech. 8, 3647–3669, 2015.
30 Pérez-Ramírez, D., Whiteman, D. N., Veselovskii, I., Kolgotin, A., Korenskiy, M., and
31   Alados-Arboledas, L.: Effects of systematic and random errors on the retrieval of particle

1   microphysical properties from multiwavelength lidar measurements using inversion with

2   regularization, Atmos. Meas. Tech., 6, 3039-3054, 2013.

3   Randles, C.A., Da Silva, A.M., Buchard, V., Colarco, P.R., Darmenov, A., Govindaraju, R.,

4   Smirnov, A., Holben, B., Ferrare, R., Hair, J., Shinozuka, Y., and Flynn, J.: The MERRA-2

5   Aerosol Reanalysis, 1980 Onward. Part I: System Description and Data Assimilation

6   Evaluation, J. of Climate, 30, 6823-6850, 2017.

7   Sugimoto, N. and Lee, C. H.: Characteristics of dust aerosols inferred from lidar depolarization

8   measurements at two wavelength, Appl. Opt., 45, 7468–7474, 2006.

9   Tesche, M., Ansmann, A., Müller, D., Althausen, D., Engelmann, R., Freudenthaler, V., and

10   Groß, S.: Vertically resolved separation of dust and smoke over Cape Verde using

11   multiwavelength Raman and polarization lidars during Saharan Mineral Dust Experiment

12   2008, J. Geophys. Res., 114, D13202, doi:10.1029/2009JD011862, 2009.

13   Tesche, M., Groß, S., Ansmann, A., Müller, D., Althausen, D., Freudenthaler, V., and Esselborn,

14   M.: Profiling of Saharan dust and biomass-burning smoke with multiwavelength

15   polarization Raman lidar at Cape Verde, Tellus B, 63, 649–676, doi:10.1111/j.1600-

16   0889.2011.00548.x, 2011.

17   Torres, O., Tanskanen, A., Veihelmann, B., Ahn, C., Braak, R., Bhartia, P.K., Veefkind, P., and

18   Levelt, P.: Aerosols and surface UV products from Ozone Monitoring Instrument

19   observations: An overview, J. Geophys. Res., 112, D24S47, doi:10.1029/2007JD008809,

20   2007.

21   Veselovskii I., Kolgotin, A., Griaznov, V., Müller, D., Wandinger, U., Whiteman, D.: Inversion

22   with regularization for the retrieval of tropospheric aerosol parameters from multi-

23   wavelength lidar sounding, Appl.Opt. 41, 3685-3699, 2002.

24   Veselovskii, I., Kolgotin, A., Griaznov, V., Müller, D., Franke, K., Whiteman, D. N.: Inversion

25   of multiwavelength Raman lidar data for retrieval of bimodal aerosol size distribution, Appl.

26   Optics, 43, 1180–1195, 2004.

27   Veselovskii, I., Kolgotin, A., Müller, D., and Whiteman, D. N.: Information content of

28   multiwavelength lidar data with respect to microphysical particle properties derived from

29   eigenvalue analysis, Appl. Optics, 44, 5292–5303, 2005.

30   Veselovskii I., O. Dubovik, A. Kolgotin, T. Lapyonok, P. Di Girolamo, D. Summa, D. N.

31   Whiteman, M. Mishchenko, and D. Tanré, 2010: Application of randomly oriented spheroids

1 for retrieval of dust particle parameters from multiwavelength lidar measurements, J.
2 Geophys. Res., **115**, D21203, doi:10.1029/2010JD014139, 2010.

3 Veselovskii, I., Whiteman, D. N., Korenskiy, M., Suvorina, A., Kolgotin, A., Lyapustin, A.,
4 Wang, Y., Chin, M., Bian, H. Kucsera, T. L., Perez-Ramirez, D., Holben, B.:
5 Characterization of forest fire smoke event near Washington, D.C. in Summer 2013 with
6 multi-wavelength lidar. Atmos. Chem. Phys. 15, 1647–1660, 2015.

7 Veselovskii, I., Goloub, P., Podvin, T., Bovchaliuk, V., Derimian, Y., Augustin, P., Fourmentin,
8 M., Tanre, D., Korenskiy, M., Whiteman, D., Diallo, A., Ndiaye, T., Kolgotin, A., Dubovik,
9 O.: Study of African dust with multi-wavelength Raman lidar during the "SHADOW"
10 campaign in Senegal, Atm. Chem. Phys. 16, 7013–7028, 2016.

11 Whiteman, D., Melfi, S., Ferrare, R.: Raman lidar system for measurement of water vapor and
12 aerosols in the Earth's atmosphere", Appl. Opt. 31, 3068-3082, 1992.

13 Wiegner, M., Gasteiger, J., Kandler, K., Weinzierl, B., Rasp, K., Esselborn, M., Freudenthaler,
14 V., Heese, B., Toledano, C., Tesche, M., Althausen, D.: Numerical simulations of optical
15 properties of Saharan dust aerosols with emphasis on lidar applications. Tellus 61B, 180–
16 194, 2009.

17 Winker, D. M., Vaughan, M. A., Omar, A., Hu, Y., and Powell, K. A.: Overview of the
18 CALIPSO mission and CALIOP data processing algorithms, J. Atmos. Ocean. Techn., 26,
19 2310–2323, 2009.

2   **APENDIX**

3   **Optical properties of aerosol components in MERRA-2 model.**

4   Table 1 summarizes the main characteristics of five aerosol components: dust, sea salt,

5   black carbon, organic, carbon and sulfates used in MERRA-2 model. For dust and sea salt five

6   size bins are considered. All values are given for the relative humidity RH=0. Thus OC, BC and

7   SU with the effective radii of 0.09 μm, 0.04 μ and, 0.157 μm respectively are presented by the

8   fine fraction only, while dust and sea salt contribute to both fine and coarse fractions.

9   The dust particles are assumed to be hydrophobic, but other aerosol components may

10   present significant hygroscopic growth. To account for the effect of relative humidity, the growth

11   factor g, which is the ratio of particle radius at current RH to the dry particle radius, is

12   introduced. Fig.A1 shows dependence of the growth factor of different aerosol components on

13   relative humidity (RH). For sea salt the results are given for five size bins from Table 1. Each bin

14   has different growth factor: g increases with increase of particle radius. Relative humidity

15   modifies also the particle complex refractive index (CRI). Dependence of the real and the

16   imaginary part of particle components on relative humidity is shown in fig.A2. For dry sea salt

17   particles RI is supposed to be the same for all size bins. However in the process of hygroscopic

18   growth the RI of different bins behaves differently: both m_R and m_I decrease with bin number

19   (radius) increasing.

2   Table 1. Parameters of the aerosol components, such as minimal radius (r_{min}), maximal radius

3   (r_{max}), effective radius (r_{eff}), real (m_R) and imaginary (m_I) part of the refractive index at 355 nm,

4   532 nm, 1064 nm used in MERRA-2 model. For dust and sea salt five size bins are considered.

5   All values are given for RH=0.

Component		r_{min}, μm	r_{max} μm	r_{eff} μm	m_{R355}	m_{R532}	m_{R1064}	m_{I355}	m_{I532}	m_{I1064}
Dust	Bin 1	0.1	1.0	0.64	1.53	1.53	1.53	0.007	0.0026	0.0022
	Bin 2	1	1.5	1.32	1.53	1.53	1.53	0.007	0.0026	0.0022
	Bin 3	1.5	3.0	2.30	1.53	1.53	1.53	0.007	0.0026	0.0022
	Bin 4	3.0	7.0	4.17	1.53	1.53	1.53	0.007	0.0026	0.0022
	Bin 5	7.0	10.0	7.67	1.53	1.53	1.53	0.007	0.0026	0.0022
Sea Salt	Bin 1	0.03	0.1	0.08	1.51	1.50	1.47	2.9E-7	1.2E-8	1.97E-4
	Bin 2	0.1	0.5	0.27	1.51	1.50	1.47	2.9E-7	1.2E-8	1.97E-4
	Bin 3	0.5	1.5	1.07	1.51	1.50	1.47	2.9E-7	1.2E-8	1.97E-4
	Bin 4	1.5	5	2.55	1.51	1.50	1.47	2.9E-7	1.2E-8	1.97E-4
	Bin 5	5	10	7.3	1.51	1.50	1.47	2.9E-7	1.2E-8	1.97E-4
OC		0.01	0.29	0.09	1.53	1.53	1.52	0.048	0.009	0.016
BC		0.01	0.29	0.04	1.75	1.75	1.75	0.46	0.44	0.44
SU		0.01	0.29	0.157	1.45	1.43	1.42	1E-8	1E-8	2.9E-6
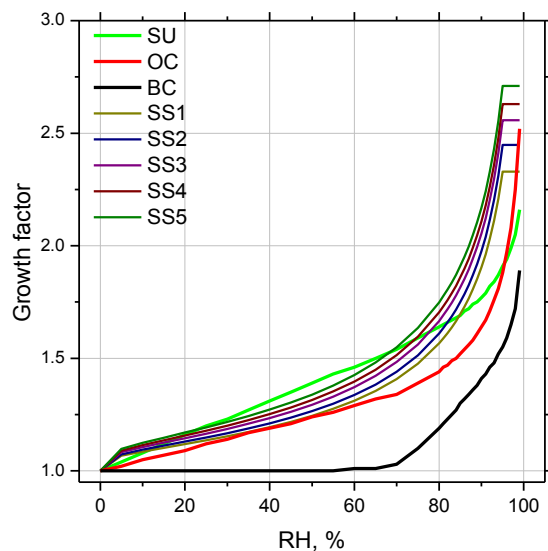
3   Fig.A1. Dependence of the growth factor of organic carbon, black carbon, sulfates and sea salt
4   on relative humidity (RH) used in MERRA-2. For the sea salt the results are given for five size
5   bins from Table 1. The growth factor increases with increase of bin number.
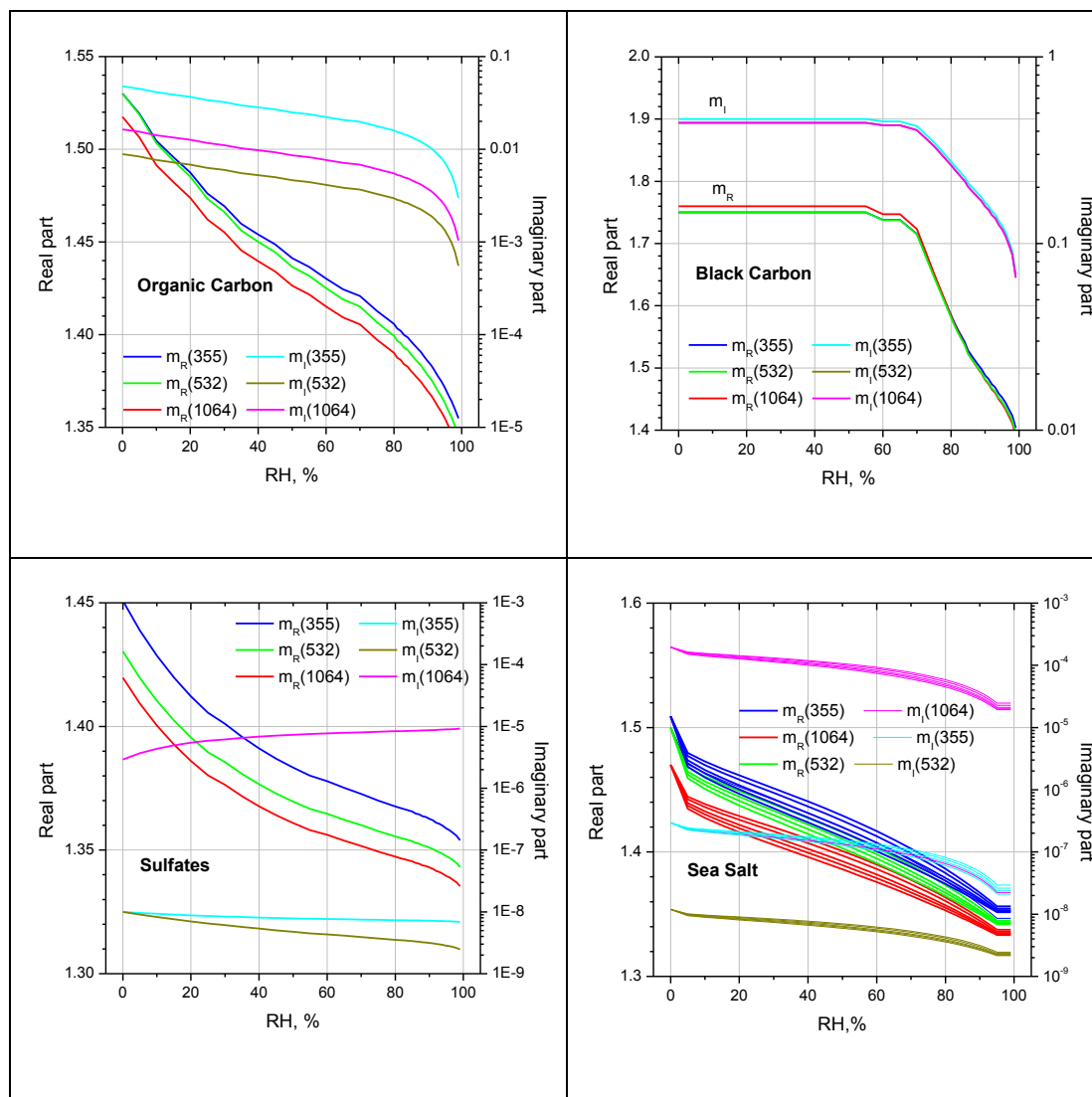
2 Fig.A2. Dependence of the real and imaginary part of the refractive index of organic carbon,

3 black carbon, sulfates and sea salt on relative humidity (RH) used in the MERRA-2 model. For

4 the sea salt the results are given for five size bins from Table 1. Both m_R and m_I decrease with

5 bin number increasing.

2   Fig.1. Five-day backward trajectories for the air mass in Mbour at altitudes 750 m, 1500 m, 3500

3   m, on 25 December 2015 at 04:00 UTC together with the map of forest fires on 20 December

4   2015.
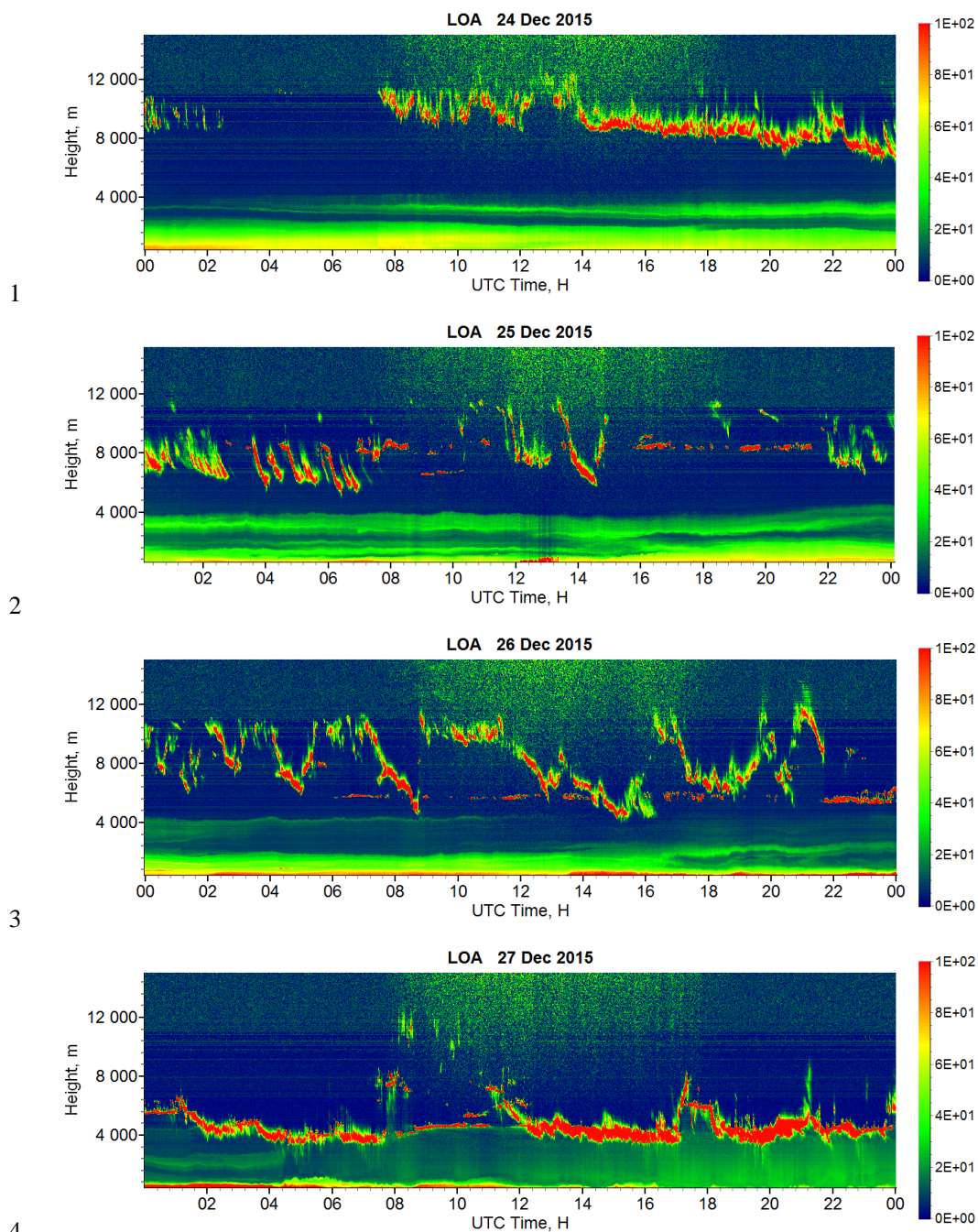
5   Fig.2. Range corrected signal of Cimel MPL for 24 - 27 December 2015.
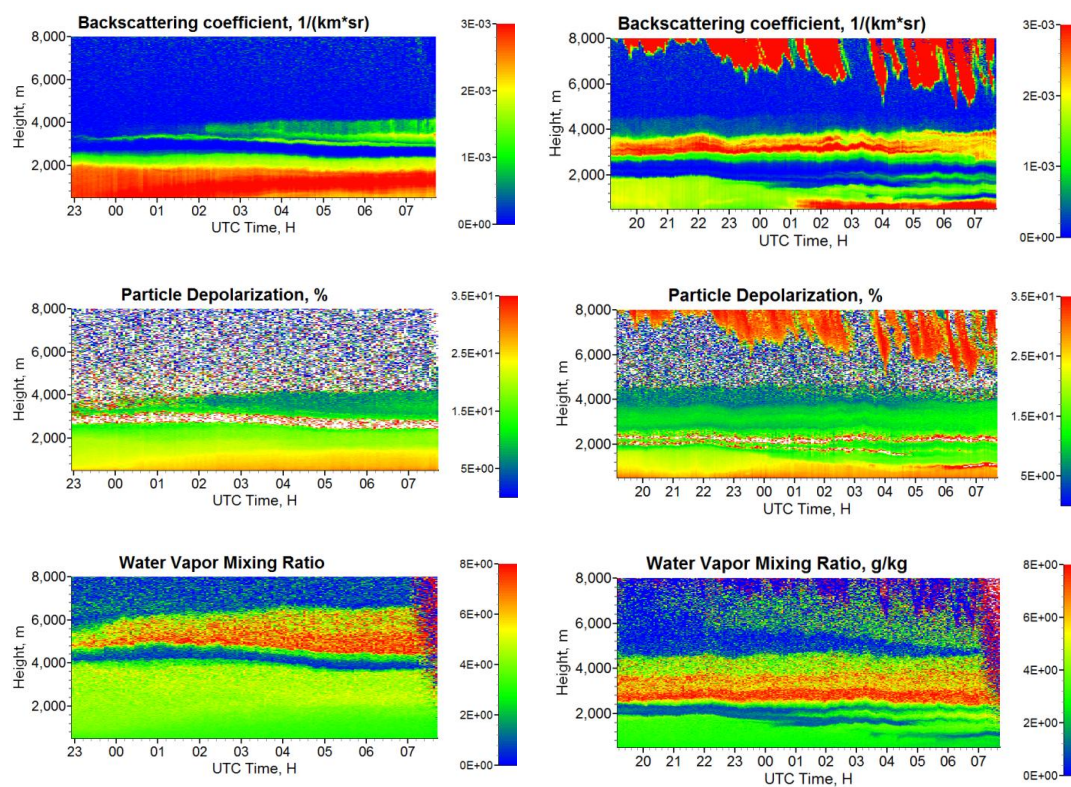
1   Fig.3 Height-temporal distributions of the backscattering coefficient and particle depolarization

2   ratio at 532 nm together with the water vapor mixing ratio derived from the Raman lidar

3   measurements on the nights 23-24 (left column) and 24-25 December 2015 (right column).

1   Time UTC
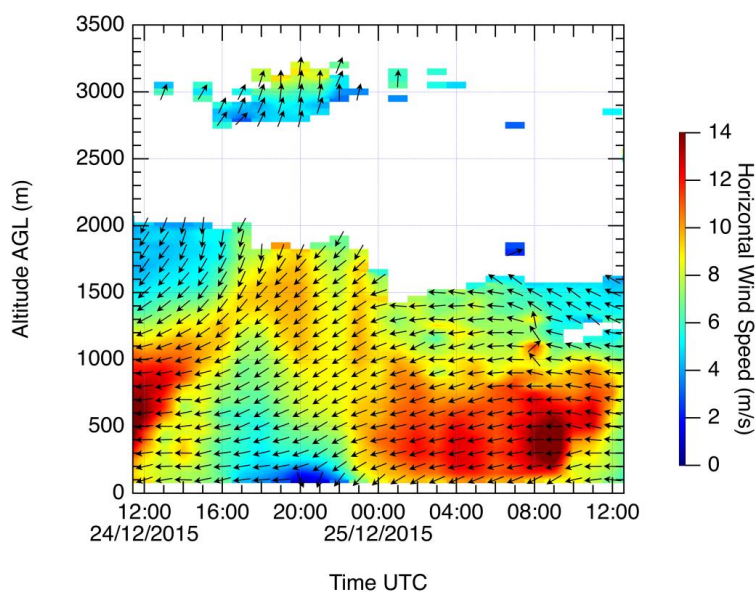
2   Fig.4. Time-height section of horizontal wind direction (arrows) and wind speed (color map)

3   deduced from Doppler lidar during 24-25 December 2015. Leftward and downward arrows

4   represent, respectively, easterly wind and northerly wind

5   Time UTC
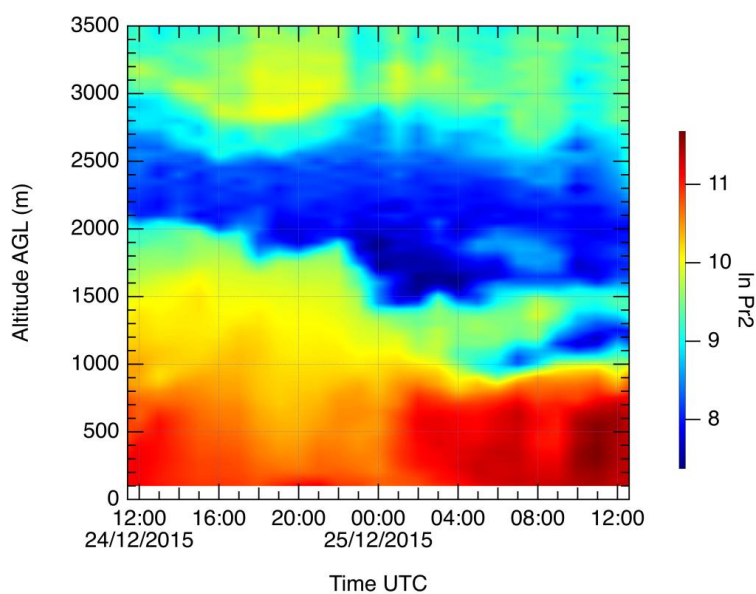
6   Fig.5. Time-height section of the logarithmic range corrected lidar signal (in arbitrary units)

7   deduced from the Doppler lidar measurements during the 24-25 December 2015 night.
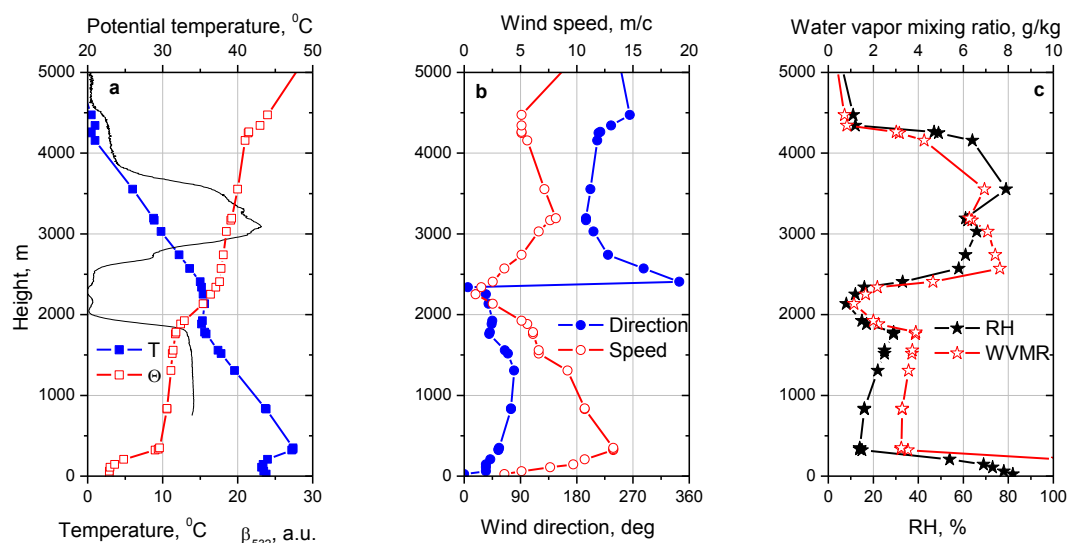
4   Fig.6. Vertical profiles of (a) temperature T, potential temperature Θ, (b) wind direction and
5   speed a   c) relative humidity RH and water vapor mixing ratio (WVMR) measured by the
6   radio sonde in Dakar at 00:00 on 25 December 201   olid line in plot (a) shows backscattering
7   coefficient at 532 nm in arbitrary units measured with e Raman lidar at 21:00 on 24 December.
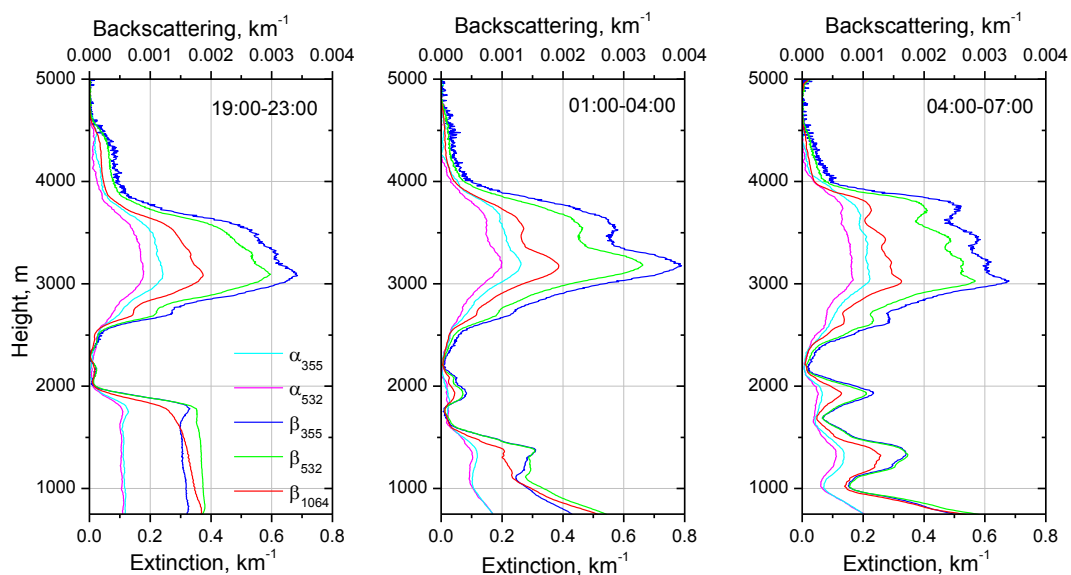
2   Fig.7. Vertical profiles of particle backscattering (β_{355}, β_{532}, β_{1064}) and extinction (α_{355}, α_{532})

3   coefficients for three temporal intervals: 19:00-23:00, 01:00-04:00 and 04:00-07:00 UTC on 24-

4   25 December 2015.
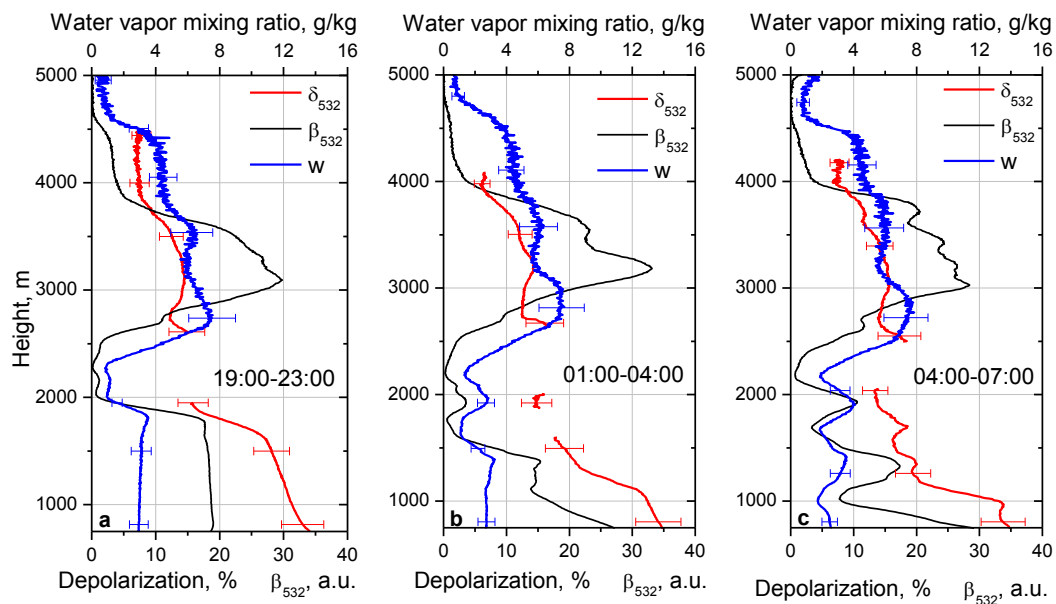
1   Fig.8. Particle depolarization ratio δ_{532} and water vapor mixing ratio w together with

2   backscattering coefficient β_{532} for the same three temporal intervals as in fig.
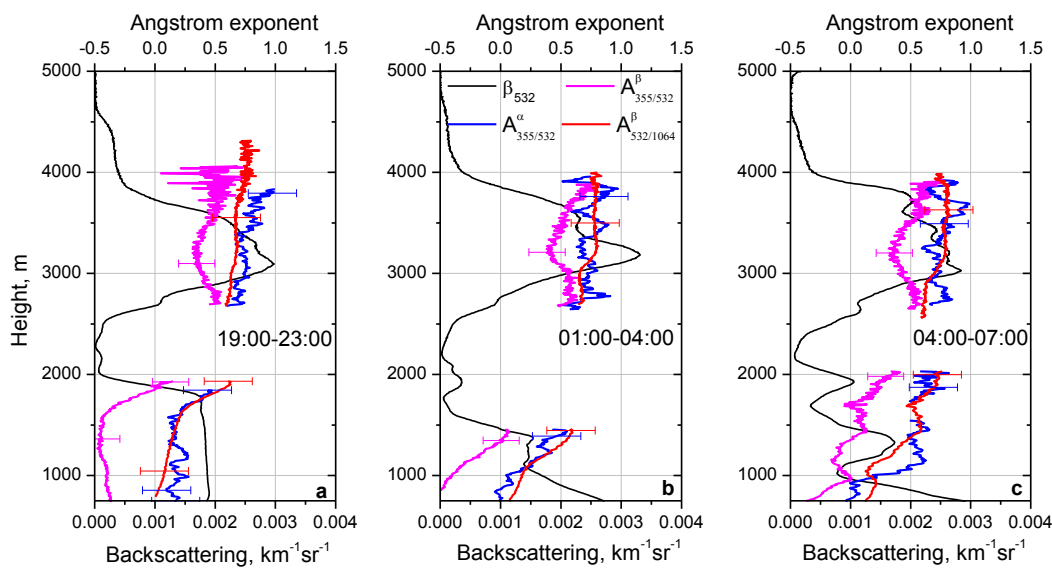
2 Fig.9 Extinction ($A_{355/532}^{\alpha}$) and backscattering ($A_{355/532}^{\beta}$, $A_{532/1064}^{\beta}$) Ångström exponents together

3 with backscattering coefficient β_{532} for the same three temporal intervals as in Fig.7.
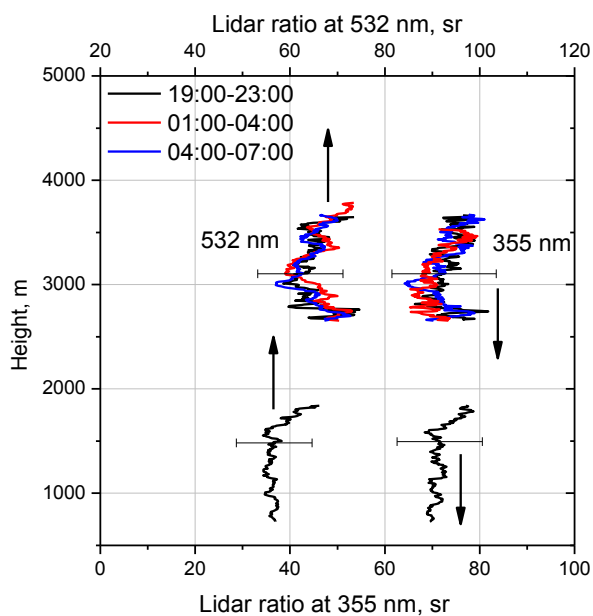
3   Fig.10. Lidar ratios at 355 nm and 532 nm for three temporal intervals from fig.7.
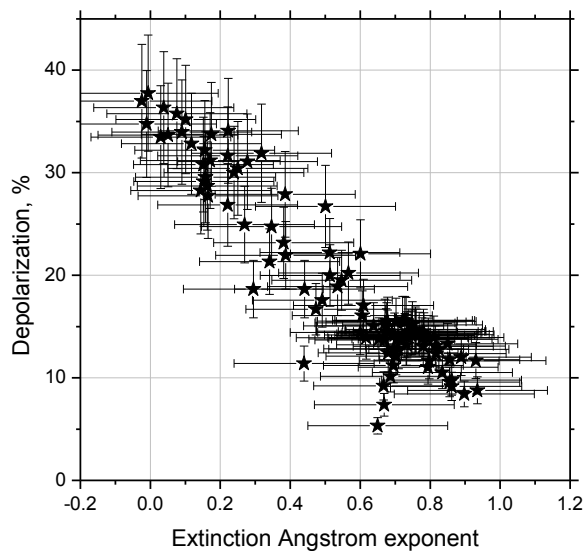
3   Fig.11. Particle depolarization ratio as a function of the extinction Ångström exponent derived
4   from data shown in fig.8, 9.
5
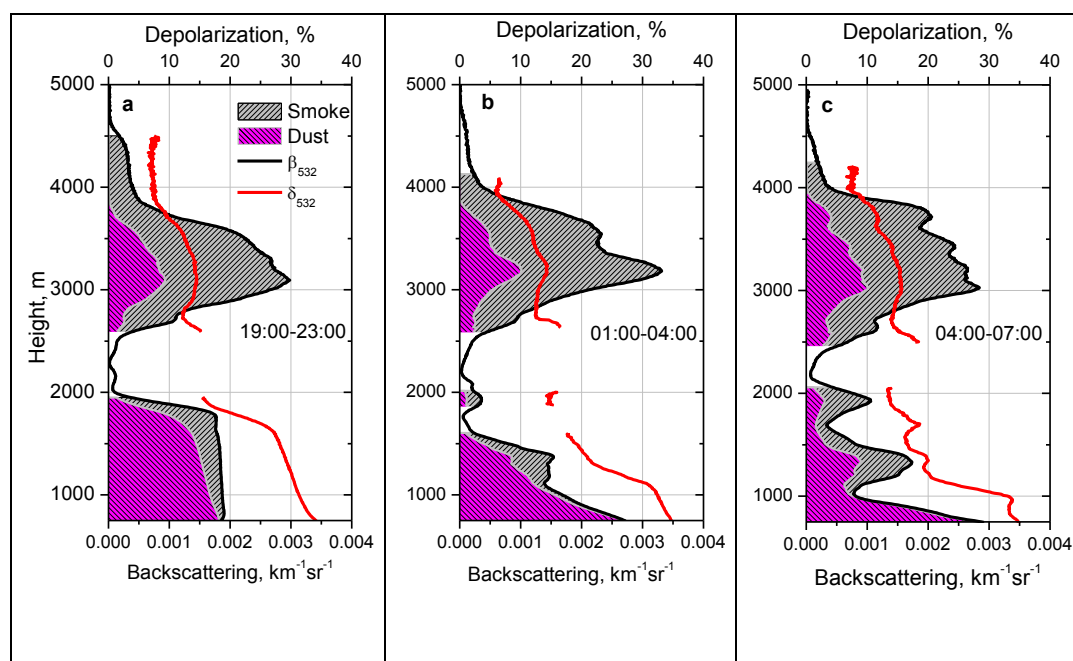
2   Fig.12. Contributions of dust and smoke to the total backscattering coefficient β_{532} together with

3   particle depolarization ratio δ_{532} for three temporal intervals on 24-25 December 2015. Magenta

4   and grey regions correspond to dust and smoke contribution to total scattering $\beta_{532} = \beta_{532}^{d} + \beta_{532}^{s}$.
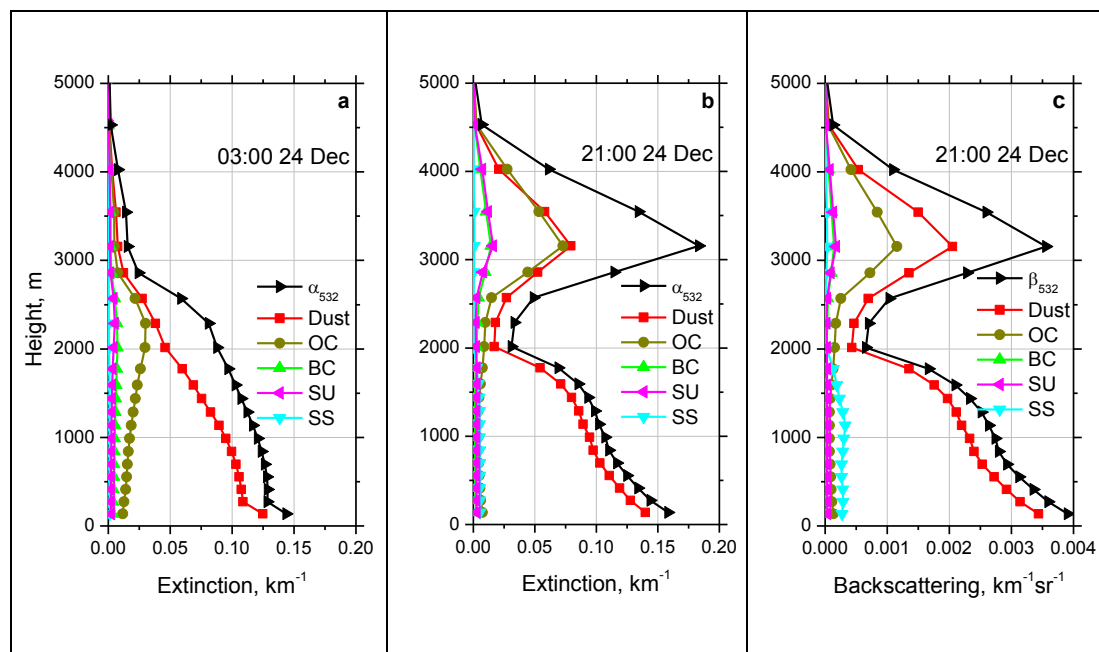
4 Fig.13. Vertical profiles of extinction coefficients at (a) 03:00 UTC, (b) 21:00 UTC and (c)

5 backscattering coefficients at 21:00 UTC on 24 December 2015 from MERRA-2 model at 532

6 nm. Profiles are given for five aerosol components: dust, black carbon (BC), organic carbon

7 (OC), sea salt (SS), sulfates (SU) together with total extinction α_{532} and backscattering β_{532}.
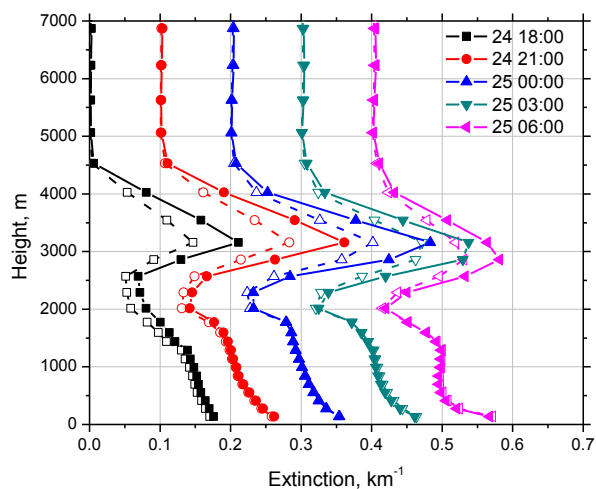
2   Fig.14. Profiles of extinction coefficient at 355 nm (solid symbols) and 532 nm (open symbols)

3   modeled by MERRA-2 on the night 24-25 December 2015 at 18:00, 21:00, 00:00, 03:00, 06:00

4   UTC. Profiles are shifted relatively to each other on 0.1 km^{-1}.
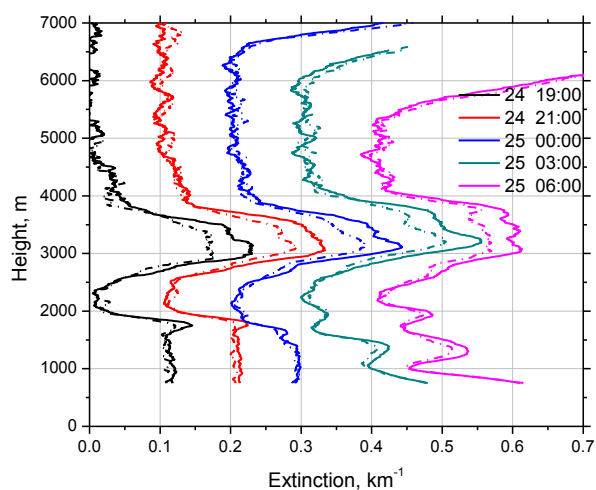
6   Fig.15. Extinction coefficients at 355 nm (solid line) and 532 nm (dash-dot) derived from Raman

7   lidar measurements on the night 24-25 December 2015. Profiles are given for temporal intervals

8   centered at: 19:00, 21:00, 00:00, 03:00, 06:00 UTC. For each profile 2 hours of measurements

9   are averaged. The profiles are shifted relatively to each other on 0.1 km^{-1}.
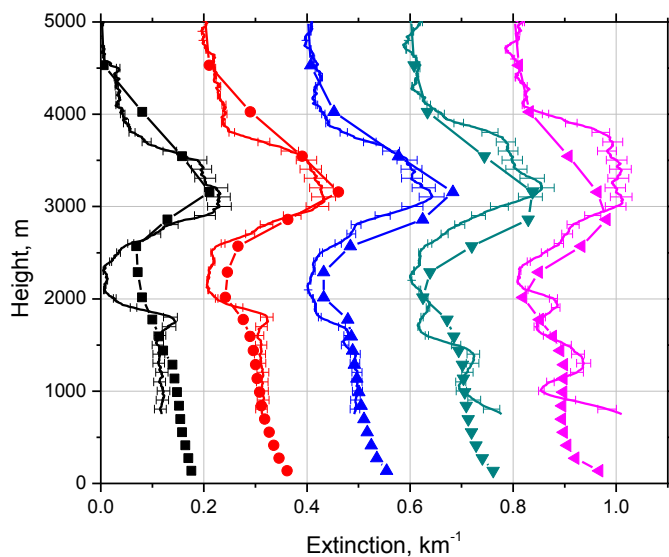
3   Fig.16. Comparison of extinction profiles at 355 nm measured by lidar (line) and modeled by

4   MESSA (line + symbols) from fig.13 and fig.14. The profiles are shifted relatively to each other
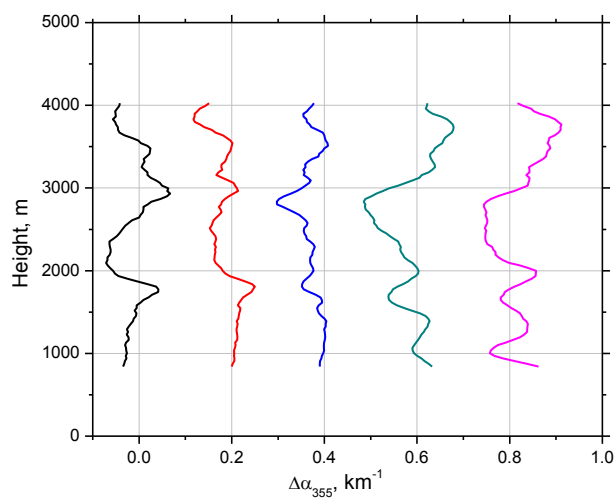
5   on 0.2 km^{-1}.

2 Fig.17. Difference between measured and modeled extinction coefficient 355 nm ($\Delta\alpha_{355}$) for

3 results shown in fig.16. The profiles are shifted relatively to each other on 0.2 km^{-1}.
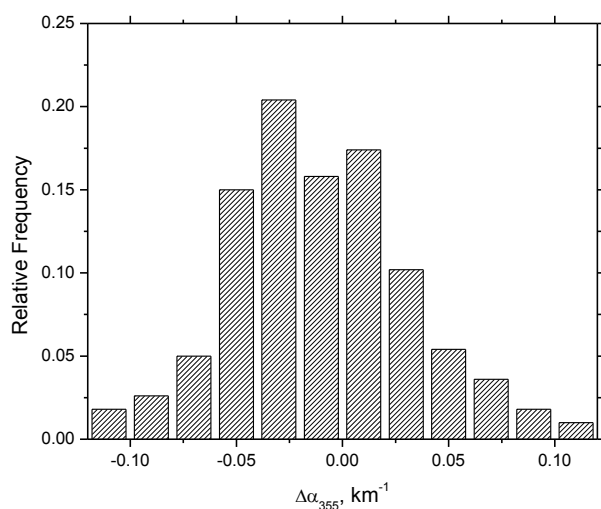
5 Fig.18. Relative frequency of $\Delta\alpha_{355}$ for profiles in fig.16. The mean value is -0.01 km^{-1} with the

6 standard deviation of 0.042 km^{-1}.
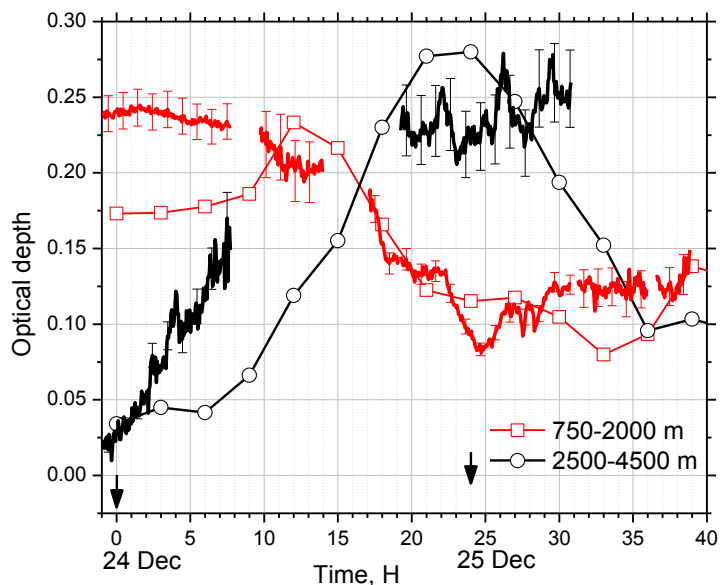
Fig.19. Optical depth at 355 nm on 23 − 24 December 2015 obtained from MERRA-2 (line +
symbols) and from the Raman lidar measurements (solid lines). The results are given for two
height intervals: 750 m − 2000 m (red) and 2500 m − 4500 m (black). Zero of time scale
corresponds to 00:00 UTC on 24 December.
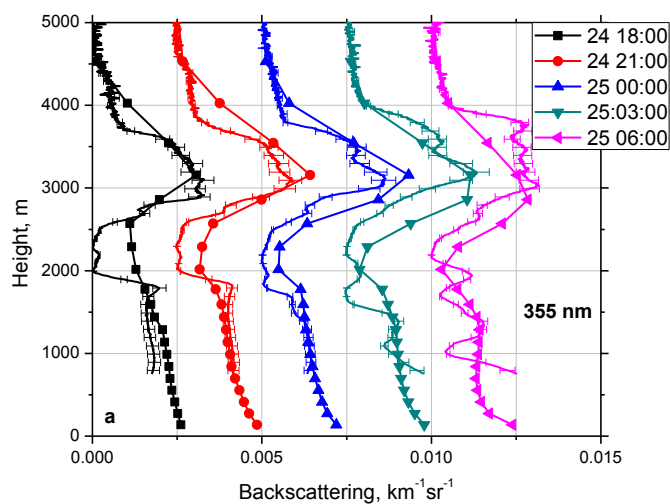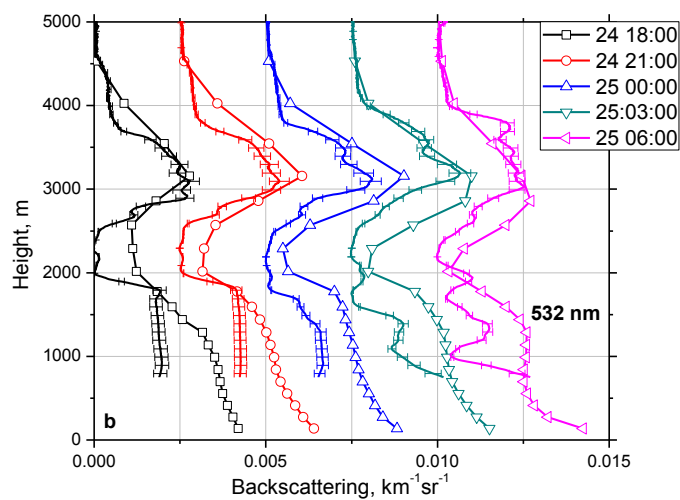
Fig.20. Backscattering coefficients at (a) 355 nm and (b) 532 nm measured by Raman lidar (solid

line) and modeled by MERRA-2 (line + symbols) on the night 24-24 December 2015. Profiles

are shifted relatively to each other on 0.0025 km⁻¹sr⁻¹. The temporal intervals are the same as in

fig.14, 15.
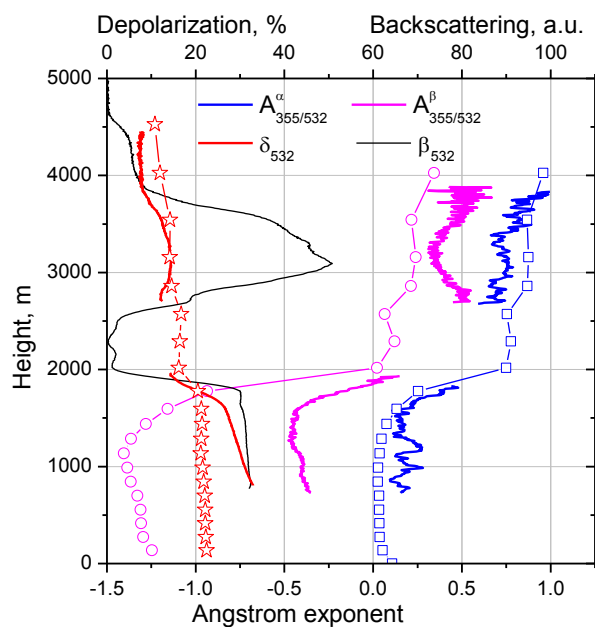
3   Fig.21. Extinction ($A^{\alpha}_{355/532}$) and backscattering ($A^{\beta}_{355/532}$) Ångström exponents together with the

4   particle depolarization ratio δ_{532} obtained from lidar measurements (line) and from MERRA-2

5   modeling (line + symbols). Lidar data are averaged over 19:00 – 23:00 UTC period while model

6   data are given for 21:00 UTC.
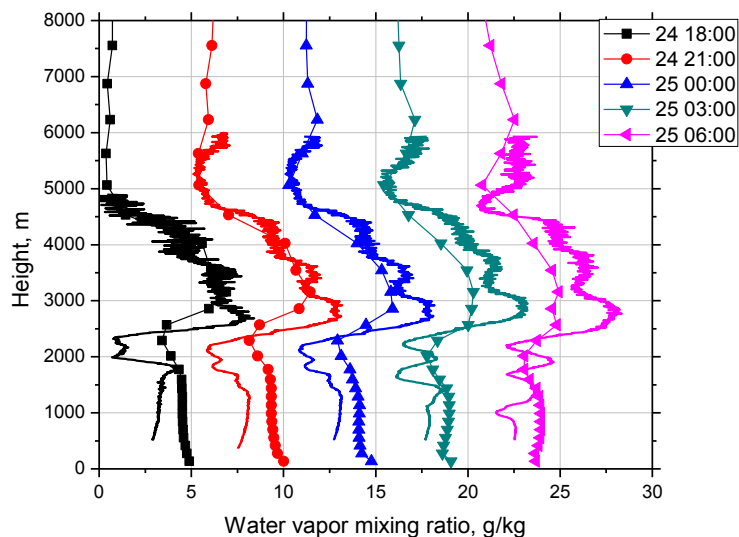
3   Fig.22. Water vapor mixing ratio derived from Raman lidar measurements (solid line) and

4   obtained from the model (line + symbols) on the night 24-25 December 2015. Temporal intervals

5   are the same as in fig.14. The profiles are shifted relatively each other on 5 g/kg.
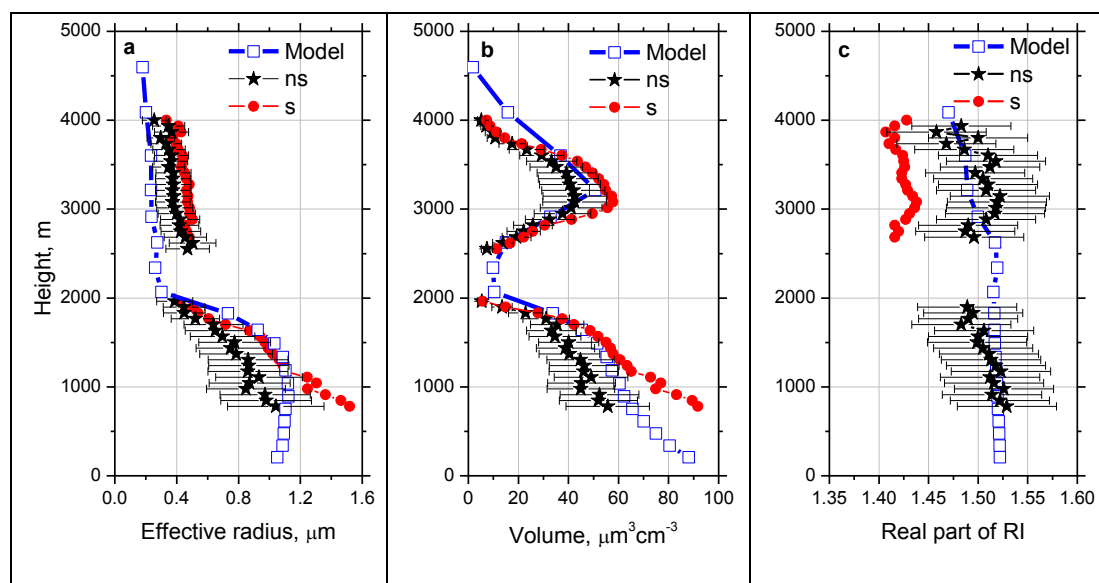
4 Fig.23. Profiles of (a) effective radius, (b) particle volume and (c) real part of the refractive index

5 derived from lidar measurements (solid symbols) and provided by MERRA-2 (open symbols).

6 Inversion of lidar measurements was performed in assumption of spherical particles (s) and using

7 the model of spheroids (ns).
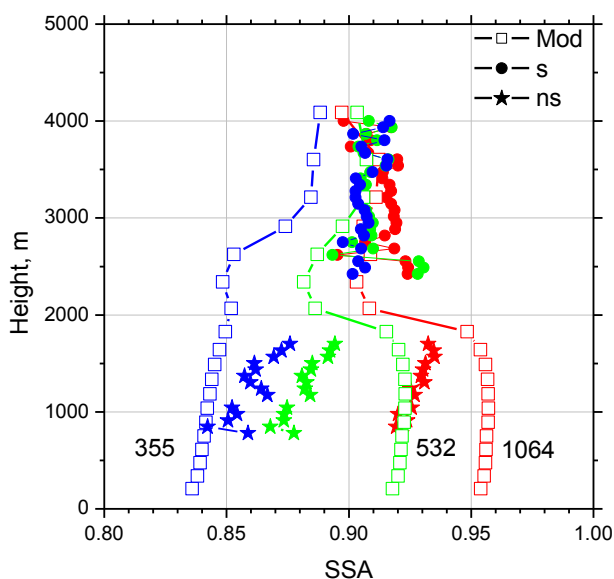
Fig.24. The single scattering albedo at 355 nm (blue), 532 nm (green) and 1064 nm (red) on 24

December 2015 retrieved from 3β+2α lidar measurements (solid symbols) and provided by the

MERRA-2 model (line + open symbols). For inversion of lidar data the spheroids (ns) were used

below 2000 m and spheres (s) above 2000 m. Lidar measurements are averaged over 19:00-

23:00 UTC interval 2015, while model data are shown for 21:00 UTC.